Design and Implementation of a High-Speed Solid-State Acousto-Optic Interference Pattern Projector for Three-Dimensional Imaging

by

Daniel L. Feldkhun

Submitted to the Department of Electrical Engineering and Computer Science
in partial fulfillment of the requirements for the degree of
Master of Engineering in Electrical Engineering and Computer Science
at the
Massachusetts Institute of Technology
Spring 1999

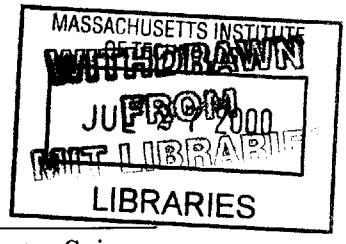

Author_____
Department of Electrical Engineering and Computer Science
Spring, 1999

Certified by_____
Lyle G. Shirley
MIT Lincoln Laboratory Research Staff
Thesis Supervisor

Certified by_____
Dennis Freeman
Associate Professor in Electrical Engineering
Thesis Supervisor

Accepted by_____
Arthur C. Smith
Chairman, Department Committee on Graduate Theses

Design and Implementation of a High-Speed Solid-State Acousto-Optic Interference Pattern Projector for Three-Dimensional Imaging

by

Daniel L. Feldkhun

Submitted To The Department Of Electrical Engineering And Computer Science

Spring 1999

In Partial Fulfillment Of The Requirements For The Degree Of
Master Of Engineering In Electrical Engineering And Computer Science

Abstract

A novel method of projecting interference patterns using acousto-optics has been developed and implemented in the context of the Accordion Fringe Interferometry (AFI) three-dimensional measurement technique developed at MIT Lincoln Laboratory. AFI is an active technique that relies on projecting interference fringes and triangulation to recover range information. AFI is suitable for a wide range of applications, and the solid-state acousto-optic interference fringe projector offers the combination of speed, robustness, and portability that can make AFI a very powerful tool for applications like machine vision, hand-held 3D scanning, high-throughput quality control systems, and motion study and modeling. This work presents the theory of acousto-optic devices and addresses design considerations for an acousto-optic AFI system. Moreover, a prototype is constructed and evaluated, and an algorithm is implemented to reconstruct the 3D surface of an object. The results indicate that an acousto-optic AFI system is practical and has high potential for applications that require high speed and portability from a 3D imaging system.

Thesis Supervisor: Lyle G. Shirley
Title: MIT Lincoln Laboratory Research Staff

Thesis Supervisor: Dennis M. Freeman
Title: Associate Professor in Electrical Engineering

Acknowledgements

I would like to thank everyone at the Laser Speckle Lab for creating a friendly and pleasant atmosphere to work in. I'd like to thank Dr. Shirley for his continued direction and his support in my accelerated quest to graduate. I am also in debt to Prof. Freeman who despite a plethora of theses, conferences, and management responsibilities, has taken time to offer help and advice when I needed it the most. I thank Michael Mermelstein for his invaluable counsel and creativity throughout this project and for all he has taught me about life, science, and the pursuit of happiness. I would also like to thank my parents for believing in me and providing much needed emotional support and inspiration. Finally, I am grateful to MIT Lincoln Laboratory and the MIT Department of Electrical Engineering and Computer Science for supporting me in the course of this work.

Table of Contents

List of Figures

Chapter 1

Introduction

1.1 Motivations for developing a high-speed three dimensional imager

The electronic age has revolutionized our ability to learn and communicate. While humans have long known how to write manuscripts and draw pictures, the amount of information that we can now record and express using audio and video technologies is unprecedented. Furthermore, the advents of telephone, radio, television, and data communications networks, have made access to such information increasingly integral to our lives. Computers are rapidly increasing our capacity to store, process, and digest this information.

As desktop computing power is skyrocketing, it is becoming ever easier to visualize three-dimensional objects without having to leave our chairs. Whether it is a building or a bug, with a click of a button we can view it from any angle, choose any desired lighting environment, zoom into any crevice, and explore the object much quicker and more thoroughly than two-dimensional images, or even movies, ever allowed. When it comes to recording the three-dimensional world, however, for the most part we are still

at the level of a painter or a scribe. While 3D imaging tools are available in narrow circles, they are often costly, cumbersome, and slow to use.

Accordion Fringe Interferometry (AFI), developed at MIT Lincoln Laboratory ([1],[2]) is a non-contact metrology method that can produce accurate three-dimensional surface maps of objects of various size, shape, and texture, without the complexity or processing requirements inherent in many other 3D measurement techniques. Thanks to a recent invention, described in Chapter 3, it is now possible to implement AFI without moving components and with full electronic control, enabling robust, high-speed, and portable 3D imaging. Such a solid-state system could be of value to a host of research, consumer, and industrial applications, some of which are listed in Figure 1.1.

The tasks of object identification, navigation, and positioning stand to benefit from a rapidly updated 3D model of the environment. A rover traveling on unknown terrain that is capable of robust 3D imaging, for example, would be faster, more accurate, and more autonomous than its 2D counterpart. Combining modern stereo-vision algorithms and technology with true 3D sensing capability would result in an even more powerful machine-vision system. A video-rate 3D imager with a tactile interface may help a blind person to navigate and interact with the world by feeling the shapes of remote objects without actually touching them. Real-time non-contact 3D sensing could also help a surgeon position his instruments more precisely during an operation.

Object scanning is another area that can benefit from high-speed 3D imaging. Hand-held 3D scanners can be useful for evidence collection in forensics, or even for consumer applications such as 3D photography, graphic art, and entertainment. Because

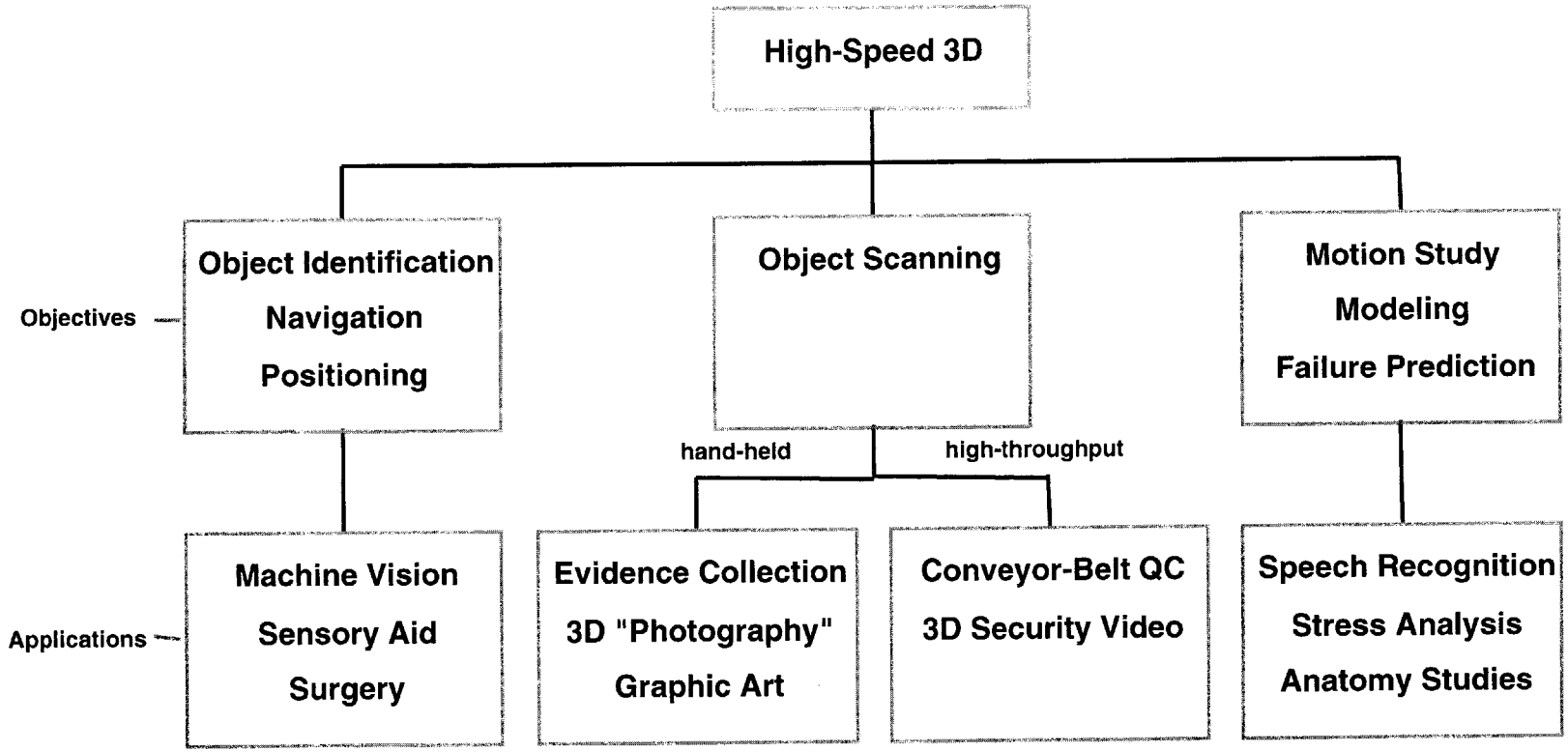

Figure 1.1 Example applications for high-speed 3D imaging

hand-held devices tend to shake, fast acquisition times are necessary. Other applications, such as quality control on a factory conveyor belt, look at moving objects and require high throughput from the 3D imaging system. Law enforcement is another possible application in which 3D reconstruction of faces, property, and crime scenes can be helpful.

The study and modeling of motion is important in a number of research areas. An accurate 3D model of a person's lips during speech can offer additional insight for lip reading and speech recognition research and applications [3]. As another example, 3D visualization of surface distortions in an object under varying stress, can be used to predict and analyze failure modes of a complex mechanical system.

1.2 Brief survey of 3D imaging technique

Although there are relatively few 3D measurement systems in production, there is a plethora of 3D measurement techniques present in the literature [4]. First, one must differentiate between *contact* and *non-contact* techniques. Contact 3D measurement devices, such as the Coordinate Measuring Machine (CMM), rely on physically probing the surface of an object. Although CMMs are common in industry, these highly accurate machines are generally very slow, cumbersome, and limited in the extent and nature of the objects they can measure. Of more relevance to this thesis work are non-contact techniques which analyze the reflected light from a distant target.

Non-contact *direct* 3D measurement techniques can be either *active* or *passive* and rely on either *triangulation* or *time-of-flight* to determine the depth of the target [5].

Passive techniques rely on ambient light reflected from the surface of an object. Stereo vision is a familiar example of a passive triangulation-based method, where the distance to a point in space viewed from different angles by two detectors can be determined using the law of cosines. Although humans are very adept at using stereo vision to perceive the 3D world, this task is much more daunting for machines. At the heart of the matter is the *correspondence problem*: the difficulty of reliably matching points in the two stereo images. This task requires highly intelligent (and compute-intensive) algorithms, that rely on high-contrast features in the images, and can be easily confused by angle-dependent variation of surface reflectance of the object.

Active triangulation-based techniques solve the correspondence problem by projecting structured light onto the object. In this case, since the spatial distribution of the illumination is known, only a single detector is necessary to triangulate the position of a given illuminated point. A simple example of a structured light technique is point triangulation, where a focused laser beam is serially scanned across the object [6]. Since the laser beam direction relative to the detector is known at any instant of time, the 3D location of the illuminated point can be determined. Other structured light techniques project more complex patterns to parallelize the measurement process, using cylindrical lenses, slits, or even coded masks on a slide projector. Related to the AFI technique discussed in this thesis, is the Moiré Interferometry method [7]. Moiré Interferometry relies on two identical gratings, one at the source and one at the detector to superimpose an interference fringe pattern onto the image of the object. The phase of these fringes can be unwrapped via image processing and used to extract the depth of the object via triangulation. All structured light techniques, however, suffer from the problem of

specular reflection. A mirror-like surface, for example, may direct the projected light away from the detector, resulting in no data, or worse, deflect the light onto other areas on the surface, resulting in an erroneous measurement. In addition, many active techniques rely on mechanically scanning laser beams or patterns, and are slow as a result. Furthermore, common to all triangulation techniques is the problem of *missing data* that results from shadowing. While shadowing can be reduced by shortening the baseline between the two triangulation elements, this also results in increased measurement errors.

Time-of-flight techniques, on the other hand, avoid the missing data problem by co-locating the detector and the projector. The most straight-forward time-of-flight technique measures the round-trip time of a reflected laser pulse, although the high temporal resolution required from the detector and the associated electronics makes such range-finders expensive and typically limits the resolution to a few centimeters. Continuous-wave time-of-flight approaches that rely on amplitude or frequency modulation also exist and greatly improve on this resolution. However, phase ambiguity problems and long exposure times necessary to reduce photon noise currently limit the range of applications for such techniques [5] .

A host of *indirect* 3D measurement methods also exist that obtain the relative shape of the object, not an absolute depth measurement. These techniques typically rely on cues like reflectance properties of the object, focus of the image, perspective, or texture gradients, and generally work for only a narrow range of objects and environments.

Despite the abundance of 3D measurement techniques, no prominent versatile approach suited for a wide range of applications has so far emerged. Accordion Fringe Interferometry, developed at MIT Lincoln Laboratory, is a structured light technique that has been used to reconstruct surfaces of objects in a wide range of sizes, shapes, and textures. It is also robust against errors, simple to implement, inexpensive, and can be made portable and fast with the technology presented in this work.

1.3 Background of the Laser Speckle Laboratory

Much of this thesis represents work done at the Laser Speckle Laboratory, part of Group 35 of the MIT Lincoln Laboratory. The Laser Speckle Lab (LSL), which was formed in 1990 under the leadership of Dr. Lyle Shirley, develops novel measurement techniques using patterns produced by interference of coherent light. While its initial work was aimed at laser speckle pattern sampling ([8], [9],[10],[11]) for target identification in missile defense, in recent years the group's focus evolved towards three-dimensional industrial metrology applications. A number of interferometric methods have developed in the process, with Accordion Fringe Interferometry (AFI) ([1],[2]) representing the latest, simplest, and perhaps most promising non-contact technique for acquiring three-dimensional surface maps of opaque objects.

In its latest incarnation, the AFI system at LSL has proven to be of high interest to the automotive and aeroplane industries for measuring large panels in process control. Such applications require a highly robust, large-scale system, capable of micron-scale resolution over a large area of coverage. There are a host of other applications, however, that do not require the high resolution or the large scale of an industrial apparatus, but

stand to benefit from the simplicity and low processing requirements of AFI. This thesis represents an effort to adapt the AFI technique to areas in research and medicine that would benefit from a high-speed, portable, and economical 3D imaging system.

Chapter 2

Accordion Fringe Interferometry

2.1 "Painting the world with fringes"

Accordion Fringe Interferometry ([1],[2]) is related to the category of 3D triangulation methods that rely on projecting "structured light" onto the target. Like the majority of structured light techniques, AFI requires only a single detector to triangulate range information about the illuminated target, whereas stereo triangulation systems need to match images from several detectors, and as a result rely on complex shape recognition algorithms that are sensitive to angle-dependent reflectivity of the target [5].

However, unlike most structured light methods which generate patterns using masks at the focal plane or using light-shaping optics, AFI relies on the interference of coherent light to "paint the world with interference fringes". As illustrated in Figure 2.1, two laser beams are focused by a lens into two "source points" at the focal plane. After the focal plane, the two beams diverge and eventually overlap to form the sinusoidal interference pattern. The density of the interference fringes projected onto a given plane

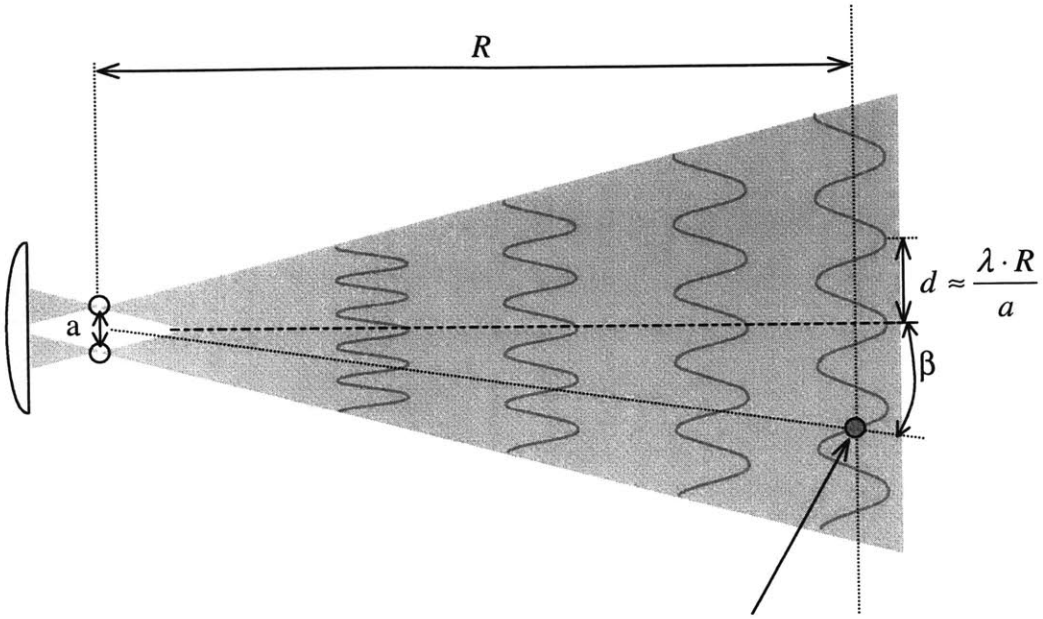

Figure 2.1 Fringe Space

in this "fringe space" depends on the distance of the plane from the focal plane and on the spatial separation of the two source points:

$$d \approx \frac{\lambda \cdot R}{a}$$

Here d is the spacing of the fringes, λ is the optical wavelength, R is the distance from the focal plane to the given interference plane, and a is the separation of the two source points. The spatial phase of the global fringe pattern can also be varied by changing the relative phase θ of the two interfering laser beams. In fact, the intensity at a given point in the fringe space can be represented by a raised cosine function [12]:

$$I = I_0 \cdot \cos^2\left(\frac{\tan(\beta) \cdot a \cdot \pi}{\lambda} + \theta\right) + I_{DC}$$

where β is defined in the diagram, I_0 is the amplitude of the fringe pattern, and I_{DC} is the fixed background illumination level. Note that both I_0 and I_{DC} will change as the laser light intensity, background illumination level, and surface reflectivity vary across the object, and as the path difference between the interfering beams approaches the coherence length of the laser light. The raised cosine term in the equation, however, depends only on the location in the fringe space and on the controllable parameters of the AFI system.

The following sections describe two related ways of extracting depth information about a given point in the fringe space. Both approaches recover the angular coordinate β, and use triangulation to determine the distance from the detector to the imaged point. Spatial phase estimation relies on measuring the local spatial phase ϕ of the fringe pattern

at a fixed point source separation a. Spectral estimation looks at the local intensity variation as the point-source separation a is changed.

2.2 Depth extraction through spatial phase estimation

As shown in Figure 2.2, by measuring the wrapped phase of the fringe pattern imaged by a pixel in a CCD array (90° in this case), one can isolate several discrete locations along the line of sight of the pixel where the imaged region of the object might lie. One way of determining the spatial phase at a given pixel is shown in Figure 2.3. As information theory dictates, by taking three measurements of a sinusoid of known frequency (determined by the point source separation in this case), one can determine all three of its *unknown* parameters – amplitude, offset, and phase (with a 360° ambiguity). This can be done robustly by shifting the phase of the entire projected fringe pattern, and measuring the corresponding intensities at each pixel *independently*. As shown in Figure 2.3, an even sampling and a simple formula results from ±90° phase shifts of the fringe pattern. Since only the spatial phase is of interest for triangulation, the amplitude and offset parameters are not explicitly calculated.

In order to disambiguate between the possible locations of the imaged point in the fringe space, we must unwrap the measured phase. One way to achieve this is to project larger "reference" fringes onto the object. This is shown in Figure 2.4. If a reference fringe is large enough to cover the entire depth extent of the object, then the phase measurements with the finer fringes can be completely unwrapped. On the other hand, a small phase measurement error of a reference fringe that is too large may result in a 360° phase unwrapping error. Thus, the noise present in the data limits the maximum ratio

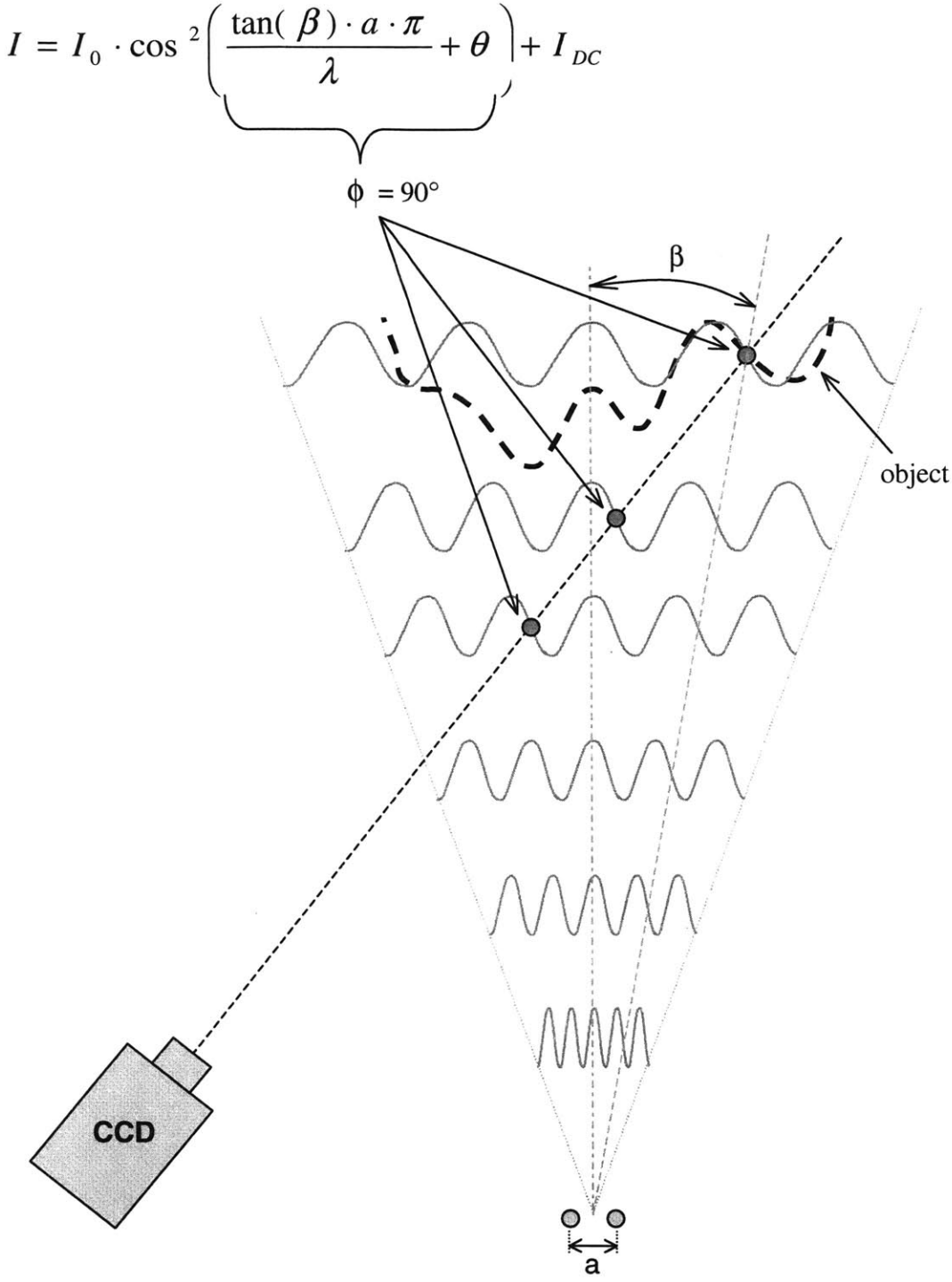

Figure 2.2 Mapping fringes to depth using spatial phase estimation

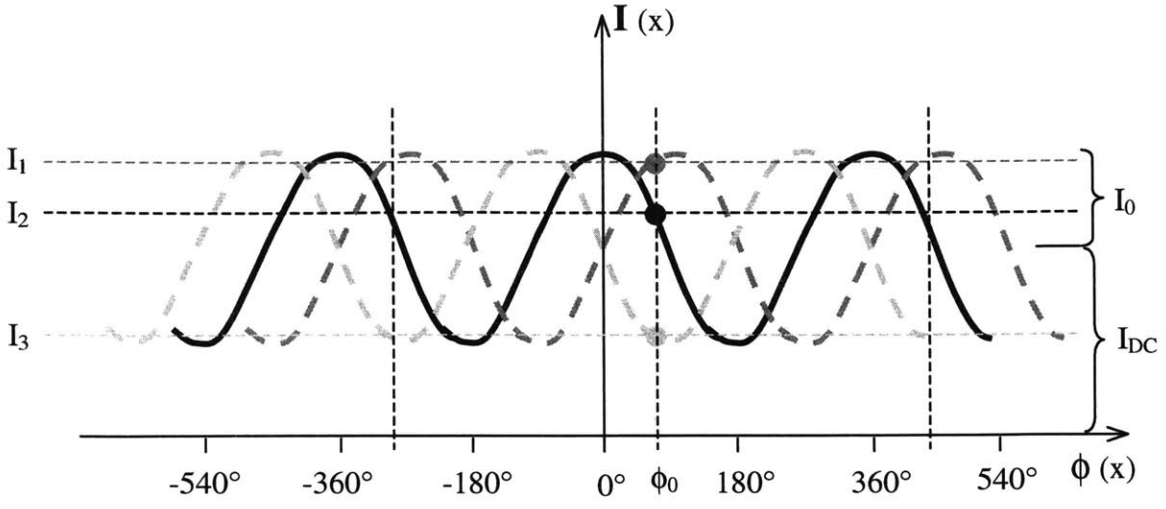

$$\left.\begin{aligned} I_1 &= I_{DC} + I_0 \sin\phi_0 \\ I_2 &= I_{DC} + I_0 \cos\phi_0 \\ I_3 &= I_{DC} - I_0 \sin\phi_0 \end{aligned}\right\} \qquad \boxed{\phi_0 = \tan^{-1}\left(\frac{I_1 - I_3}{2I_2 - (I_1 + I_3)}\right), \quad 0° < \phi \le 360°}$$

Figure 2.3 Estimating spatial phase by phase-shifting the fringes ± 90°

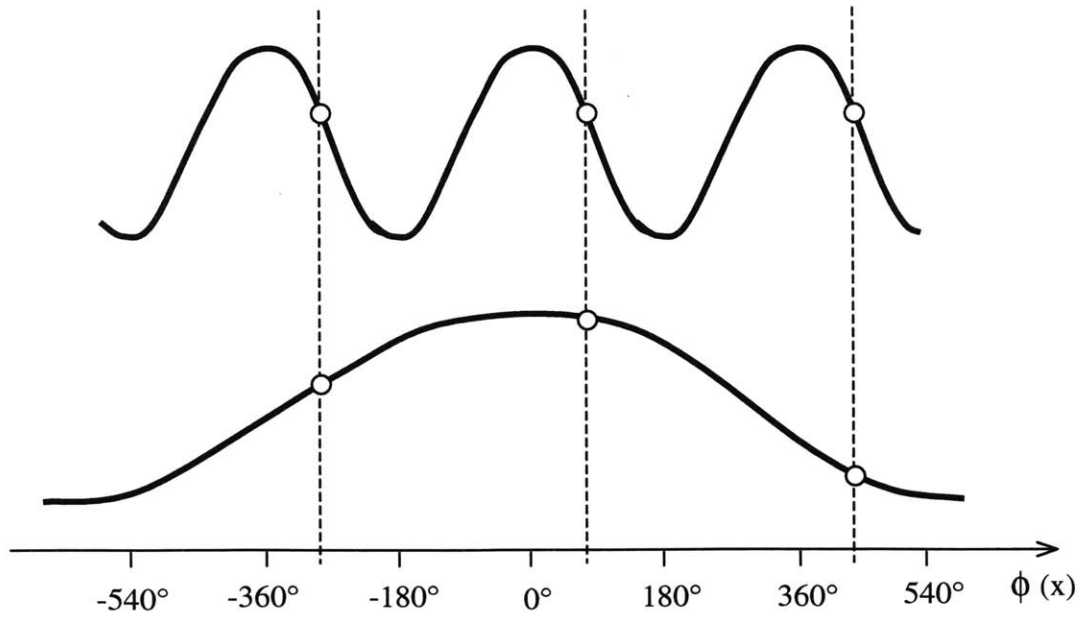

Figure 2.4 Principle of phase unwrapping using larger reference fringes

between the density of a set of fringes, and the density of the reference fringes used to unwrap them. Once the fringes are unwrapped, however, they can be used as a reference to unwrap an even more dense interference pattern. Since finer fringes result in better resolution[1], this process can be iterated until the finest fringes are unwrapped.

2.3 Depth extraction through spectral estimation

The concept of spectral estimation in AFI is illustrated in Figure 2.5. Variation in the separation of the two point-sources causes a stretching of the fringes (as in an accordion). As required by the raised cosine function, the intensity at any given point in the fringe space oscillates sinusiodally as a result, where the oscillation frequency is a function of the angle β. Thus, by determining this oscillation frequency at a given point on the illuminated object, one can extract its depth via triangulation without ambiguity (as long as the location of the null fringe is known).

One way to determine the oscillation frequency at a given point is to move the point-sources apart and count the number of fringes that pass by. This requires hundreds of image frames for a single surface reconstruction. Another tactic is to use only a few point source separations, and use a statistical minimization routine to fit a sinusoid to these samples. This approach, however, can be very computationally-intensive. As a result of these practical drawbacks, the phase estimation technique was chosen in favor of spectral estimation (at least at this stage of AFI development).

[1] This is true while the fringes are well enough resolved by the CCD [1].

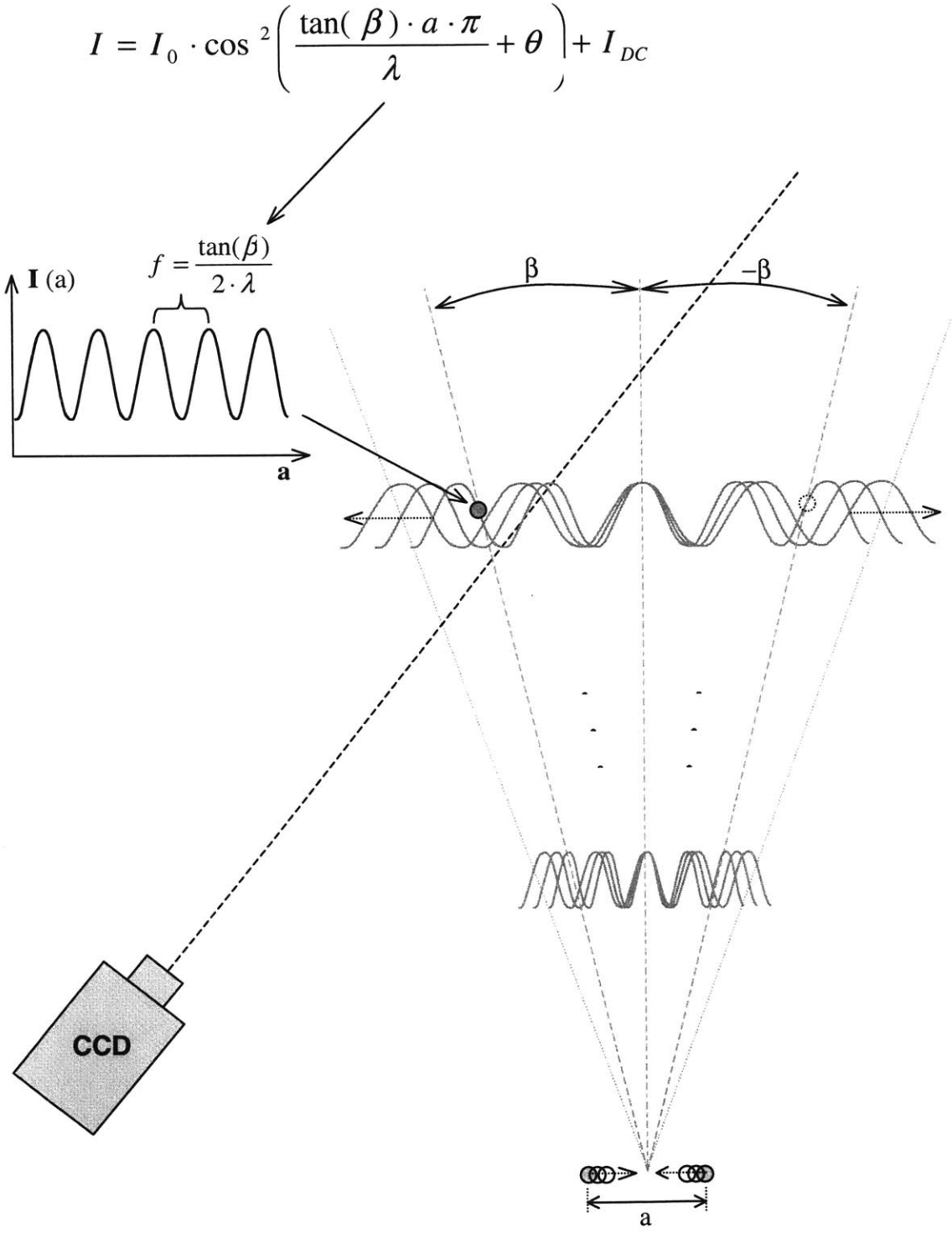

Figure 2.5 Mapping fringes to depth using spectral estimation

2.4 Benefits of AFI

Accordion Fringe Interferometry extends the state of the art in 3D measurement. Some of the benefits that AFI has to offer for a wide range of applications including high-speed and portable 3D imaging are listed below.

- *Resistant to propagation of errors:* Because phase is calculated and unwrapped for each pixel independently, errors in range estimation are confined to their corresponding pixels.
- *Well-behaved at sharp edges:* Unlike several other 3D techniques which exhibit discontinuities and other anomalies at sharp edges of the targeted object, AFI is robust against such discontinuities. Due to the unwrapping process, a phase-measurement error resulting from a sudden jump within a region imaged by a single pixel, will be confined to at most 360°. Furthermore, due to the pixel-independent phase measurement technique, any such errors will not affect neighboring pixels.
- *Insensitive to variations in illumination level:* Because triangulation depends only on the phase and frequency of the fringe pattern, variations in amplitude or bias of the fringe pattern over the extent of the object are inherently compensated for. Although intensity variations do reduce the dynamic range of the CCD available to some regions of the object, simulations have shown that the phase estimation technique is robust even with two or three bits of quantization.
- *Parallel acquisition, parallel processing:* Because all pixels are acquired simultaneously by the CCD and range is calculated independently for each pixel, this technique is fit for parallel processing. Modularity of the steps involved in measuring and unwrapping the phase also benefit computation efficiency.

- *Modest processing and memory requirements:* The computation involved in determining and unwrapping the phase for each pixel and performing a triangulation calculation is comprised of only a few dozen operations. The memory requirements are also low – at most three CCD frames need to be held in memory at once (during the phase calculation step). There is a real possibility of real-time video-rate AFI processing with dedicated hardware.
- *Simple hardware:* An AFI system consists of a CCD detector, a fringe projector, and the associated software and electronics. Most of these components are off-the-shelf items and are relatively economical.

2.5 Current state of AFI

The Accordion Fringe Interferometry technique has evolved through many iterations of method and prototype. The current AFI system is not only a successful laboratory prototype, but is being tested at a major airplane production facility to measure aircraft body panels as part of the quality control process.

One would also like to expand AFI into areas where the requirements are altogether different from industrial metrology, where more important than high resolution are low cost, speed, portability, and automation. Clearly, many 3D applications would benefit from the simplicity and robustness of the AFI method.

A recent invention which provides a solid-state method of projecting and electronically controlling interference fringes using an Acousto-Optic Modulator may be instrumental in overcoming the difficulties of bringing AFI into the world of high-speed portable 3D imaging, perhaps the next big step in its trend of evolution.

Chapter 3

Implementation of AFI projector using acousto-optics

Accordion Fringe Interferometry requires precise control over the phase and frequency of a projected interference fringe pattern. The AFI projector currently used for industrial metrology relies on translation of optical components, and its precision and speed is limited by the motion-control system. This chapter presents an alternative solid-state design of an interference fringe projector using an Acousto-Optic Modulator that is geared towards applications that require a portable high-speed 3D imaging system.

3.1 Physics of an Acousto-Optic Modulator

An Acousto-Optic Modulator (AOM), consists of a crystal in contact with a piezo-electric transducer (PZT), as depicted in Figure 3.1. By driving the PZT with a sinusoidal electric signal (typically around 100 MHz), a traveling sound wave is generated in the crystal and is absorbed by an acoustic absorber material positioned at the

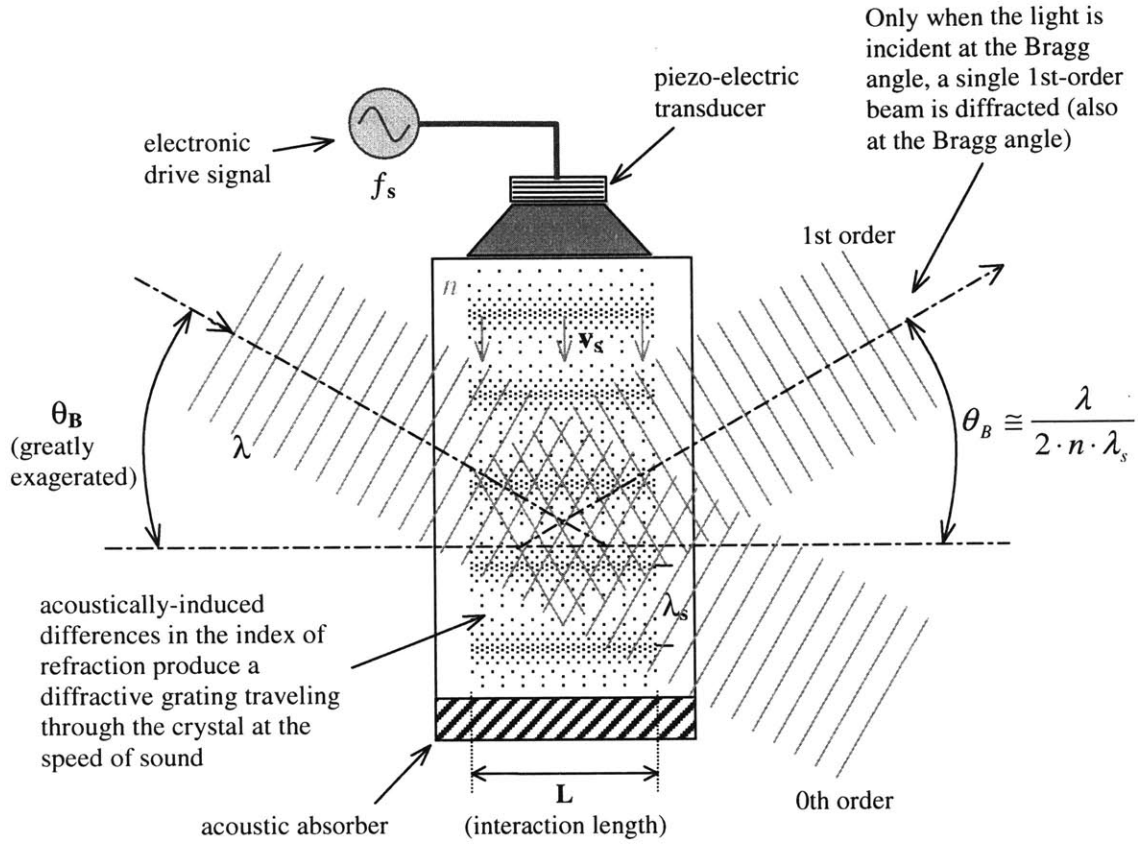

Figure 3.1 The Brillouin Phenomenon in a Bragg cell

opposite end of the crystal. When coherent light is made to pass through this excited medium, several phenomena are observed:

Bragg Diffraction

A laser beam incident on the traveling sound wave is diffracted in a phenomenon known as Brillouin scattering[13]. The combined effect of acousto-optic interaction in a material that is comprised of different scattering regions can be understood as follows.

The acoustic wave consists of sinusoidal perturbation in the density, and hence the refractive index of the material. At a given moment in time, for a sufficiently long acousto-optic interaction length L, this wavefront of index of refraction gradients can be thought of as an array of partially-reflecting "mirrors" [14]. The incident beam will be diffracted by a given mirror in this array only if all the scattering regions along the length of the mirror contribute in phase. This can happen only if the angle of incidence at each mirror is equal to the angle of diffraction (as would be expected for a mirror). Furthermore, the beam will be diffracted in a certain direction only if each mirror in the array contributes in phase with the other mirrors to the overall diffracted wavefront. These constructive interference conditions are combined in what is known as the Bragg diffraction condition:

$$2\lambda_s \sin\theta_B = \frac{\lambda}{n_0}$$

where λ_s is the acoustic wavelength within the medium, λ is the wavelength of light in free space, n_0 is the index of refraction, and $\theta_i = \theta_r = \theta_B$ is the Bragg angle (typically a few degrees). Note that due to the necessary equality between θ_i and θ_B, only the first-order

beam is diffracted under this condition, and is angularly separated from the zeroth-order beam by $2\theta_B$.

Based on the mirror model, one may wonder why θ_B can not be a multiple m of λ/n_0. While the Bragg angle is not unique for diffraction from discrete surfaces, it can be shown that due to the continuous nature of the index of refraction gradients in the crystal, m=1 is the only mode that will result in acousto-optic diffraction [14].

When the acoustic wavefront is very thin, the acousto-optic interaction length L is short and the acoustic wavefront is better modeled by an array of point scatterers rather than by an array of mirrors. Thus the phase matching condition that was used to pin the angle of diffraction to be equal to the angle of incidence for a mirror does not hold in this case, and multiple diffraction orders exist as in the familiar case of a diffractive grating. This situation is known as the Raman-Nath regime of acousto-optic interaction [15]. The transition between the Raman-Nath regime and the Bragg regime is not clear cut, but by convention is defined using the parameter Q [16]:

$$Q = \frac{2\pi \cdot \lambda L}{n\lambda_s^2}$$

For $Q < 0.1$, the operation is said to be Raman-Nath. For $Q > 4\pi$ the regime is considered Bragg. In general, Acousto-Optic Modulators are made to operate in the Bragg regime of acousto-optic interaction, where the interaction length is long, and only the first-order beam is diffracted .

Amplitude Modulation

The amplitude of the acoustic signal determines the gradients in the index of refraction in the crystal, and thus the reflection coefficients of the analogous array of mirrors. As a result, the optical energy transferred from the zeroth-order beam to the first-order beam can be rapidly and precisely controlled by amplitude-modulating the drive signal to the PZT. Typically, diffraction efficiency of ~90% and modulation bandwidth of ~1MHz can be achieved. Since the two beams can be easily separated, this effect is commonly used to modulate the intensity of a laser beam, and leads to the name of AOM.

Deflection

Another use of the AOM stems from the fact that even if the angle of incidence and the acoustic frequency do not satisfy the Bragg condition exactly, diffraction still occurs. If θ_i and λ_s do not stray too far from the Bragg condition, destructive interference only slightly dims the first-order beam. As illustrated in Figure 3.2A, however, the angle of the beam, is no longer restricted to the Bragg angle θ_B, but will deflect slightly as a function of acoustic frequency, pointing in the direction where the destructive interference is least. In fact, for small $\Delta\theta$ and θ_B, $\Delta\theta$ is related to Δf_s in an approximately linear fashion [14]:

$$\Delta\theta = \frac{\lambda \cdot \Delta f_s}{n \cdot v_s}$$

where v_s is the velocity of sound in the medium. Typically, $\Delta\theta \approx 0.5\theta_B$ can be achieved on either side of θ_B before the amplitude of the diffracted beam falls by 3dB compared to the amplitude at θ_B.

Diffraction of multiple beams

Although the operation of an AOM is best understood by studying the effects of a single sinusoidal acoustic wavefront, a superposition of several frequencies in the drive signal will result in the superposition of several acoustic wavefronts, and will generate several angularly-separated first-order beams. This effect is shown in Figure 3.2B. Since the amplitude and frequency of the drive signal can be independently controlled, so can the amplitude and direction of each of the multiple first-order beams!

Optical phase and frequency shifts

So far we have focused on the acoustic wavefront as seen by the incident laser beam at a given moment in time. Since sound propagates much slower than light, this is a good approximation for understanding the effects of acousto-optic interaction on the direction and amplitude of the diffracted beams. However, conservation of momentum requires that the traveling acoustic wavefront must also impose a unique Doppler shift $f_{si} = v_s/\lambda_{si}$ on each of the diffracted first-order beams relative to the unperturbed zeroth-order beam. In addition, the acoustic wave adds a phase shift to the diffracted optical beam, so that a relative phase shift between two superimposed acoustic waves results in the same relative phase shift between the corresponding optical beams. Both of these properties,

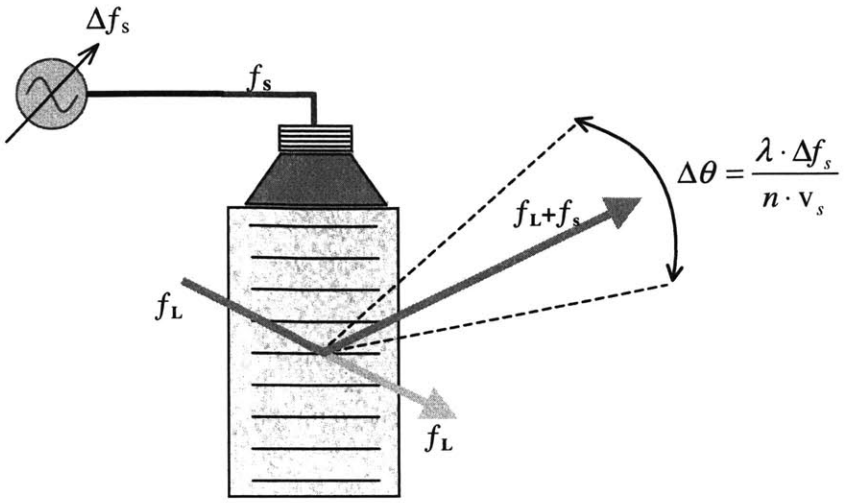

A. Direction of the 1st-order beam can be controlled by varying the acoustic frequency

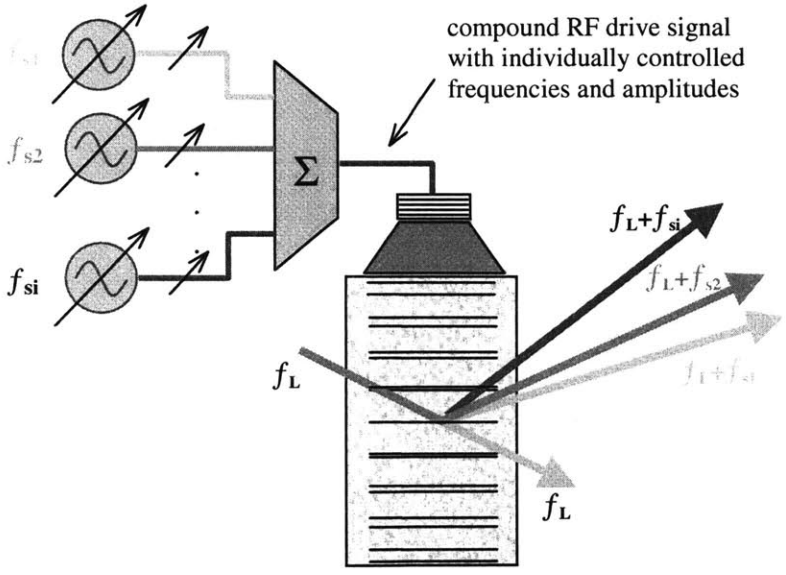

B. Multiple acoustic frequencies deflect multiple 1st-order beams

Figure 3.2 Beam deflection using an acousto-optic cell

have major repercussions for generating and controlling an interference pattern using an AOM.

3.2 Generating stationary interference fringe patterns

3.2.1 Projecting accordion fringes

As discussed in the previous section, an AOM can be used to separate a laser beam into two or more beams, and to electronically control the angular separation, amplitude, and phase of the beams. The AFI technique, however, relies on the ability to combine and interfere coherent beams near the object of interest. The simplest way to achieve this using acousto-optics is to place a lens in the path of the angularly separated beams produced by the AOM. The function of a lens is to convert angular separation between incident planar wavefronts into spatial separation at its focal plane. The separation between the corresponding focal points, or "source-points", is an approximately linear function of the angular separation of the diffracted beams, and remains the same no matter where the lens is placed in the optical path of the beams. If we choose a lens with a small enough focal length to cause the beams to overlap in the region of interest, a fringe pattern will result with the fringe spacing simply related to the source-point separation, to the angular separation, and thus to the frequency difference between the two beams.

One such arrangement is depicted in Figure 3.3. Here a superposition of two frequencies is used to drive the AOM. The compound drive signal is generated by multiplying a sinusoid with a variable modulation frequency f_m by a sinusoid with a

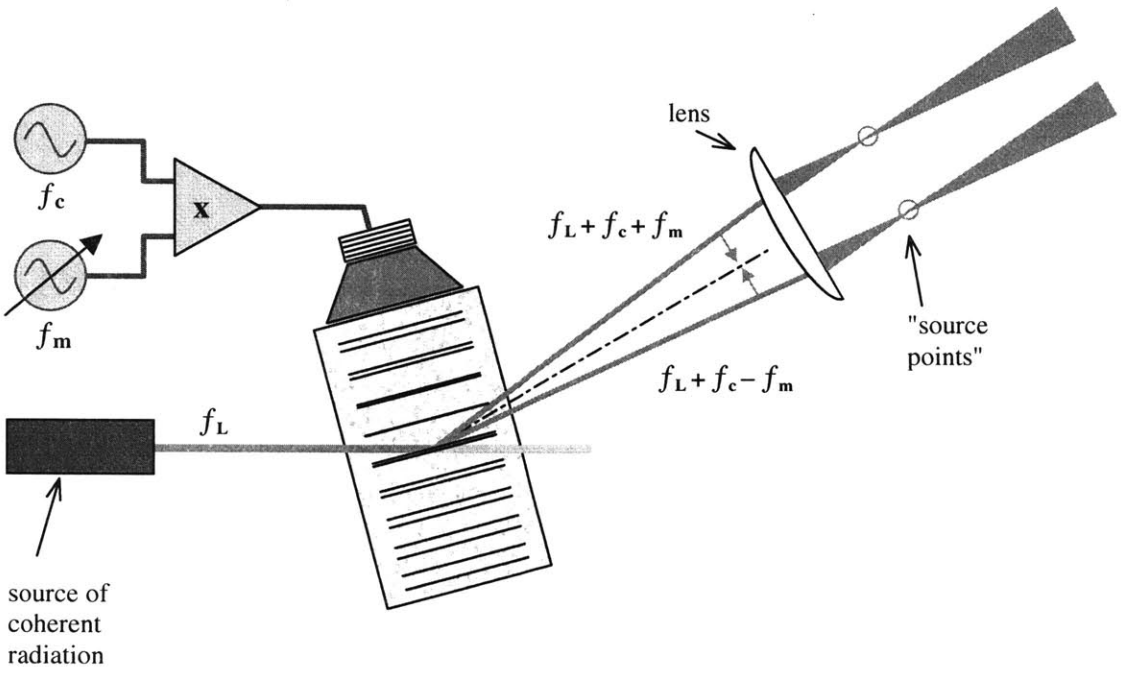

Figure 3.3 A compound-drive acousto-optic fringe projector

fixed center frequency f_c. Thus by varying f_m, the source-point separation can be adjusted about a fixed point of symmetry from zero separation to the maximum separation allowed by the bandwidth of the AOM, thereby producing accordion motion of the interference fringes.

It is also possible to generate an interference pattern using a single drive frequency by interfering the first-order beam with the zeroth-order beam. This has the advantage that a substantially (~2.5x) larger source-point separation is possible, resulting in finer fringes and better resolution. However, there are several difficulties with this approach:

- The point of symmetry of source-point motion is not fixed as it is in the compound drive case, and the null of the fringe pattern will shift as the source-points are drawn apart. This effect can be easily compensated for in the AFI mathematics.
- The lowest drive frequency allowable by the bandwidth of the AOM limits the proximity of the source points. As a result it is not possible to generate large reference fringes, calling for other phase unwrapping strategies in the AFI method.

As a consequence, the compound drive approach is currently the preferred strategy.

3.2.2 Freezing the fringes

Although the apparatus described so far causes two diffracted beams to interfere, fringes do not appear across the interference plane. The problem lies in the fact that the interfering beams have a relative Doppler shift. As a result, the light intensity at any given point on an interference plane will oscillate in time at the difference frequency as the two beams "beat" against each other. On the other hand, because the Doppler shift is

very small compared to the optical wavelength, *at any moment in time* constructive and destructive interference between the two beams still occurs across the interference plane and results in the familiar full-contrast fringe pattern. These two observations require that the interference fringe pattern travel rapidly across the interference plane, as the acoustic wave travels across the AOM. Any exposure time that is longer than the period of the traveling interference pattern (i.e. 25ns for a difference frequency of 40MHz), will show a featureless blur.

The key concept that makes the AOM technology useful for AFI is that the traveling interference fringes can be "frozen" in time at any spatial phase desired by amplitude-modulating the radiation intensity in sync with the AOM drive signal. This is illustrated in Figure 3.4. As the intensity at a given point on the illuminated object oscillates at the difference frequency of the two interfering beams, $2f_m$ in the case of the compound drive fringe projector, strobing the laser power at exactly the same frequency will "freeze" the interference pattern in time at a particular point in the oscillation[2]. The synchronization between the laser and the AOM control signals can be easily accomplished by digitally synthesizing the signals using the same reference clock, for example. The relative phase between the two interfering beams, and hence the spatial phase of the resulting fringes, can be precisely controlled either by changing the phase of the compound signal driving the AOM, or by changing the phase of the laser strobe signal. The figure shows simulated stationary interference fringe patterns that would be projected onto an object with 0°, 90°, and 180° relative phase shifts between the laser and the AOM signals.

[2] Of course, if the laser's modulation bandwidth is not high enough, one can put an electronically-controlled light amplitude modulator in the path of the laser beam instead.

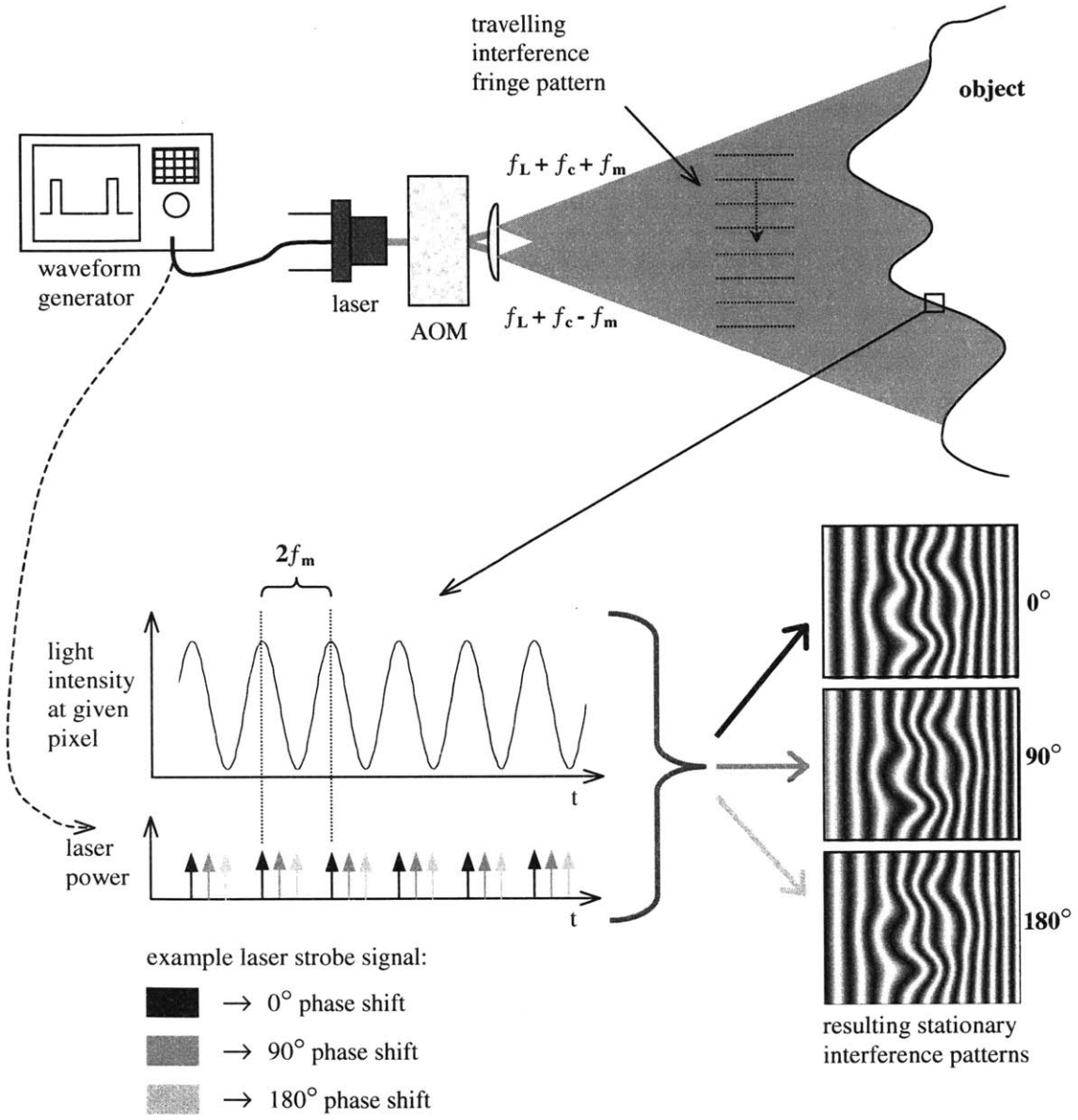

Figure 3.4 Freezing and phase shifting a traveling interference pattern

One clear disadvantage of strobing the laser is the inherent loss of light power. This is a serious issue, since the projector's light output capability limits the distance of the objects to be imaged (to a few meters in a practical case), and is a major factor in the overall cost of the system. It turns out, however, that it is not necessary to strobe the laser with short pulses to obtain a stationary interference pattern. In fact, any light intensity modulation will result in the appearance of a stationary sinusoidal fringe pattern with some contrast measure between 0% (in the case of no modulation) and 100% (in the case of modulation with a train of impulses). The choice of the modulation waveform becomes a tradeoff between the desired contrast of the stationary fringes and the power output desired from the laser. This can be understood by examining Figure 3.5.

Without any light intensity modulation, due to the traveling interference fringes, each pixel *i* of three adjacent pixels on the interference plane would see intensity oscillations $I(x_i,t)$ at the difference frequency that are out of phase with each other by a time interval $t = \Delta x/v_s$, where Δx is the separation of the pixels. The actual intensity at each point, $I(x_i)$, accumulated over the exposure time, is obtained by multiplying $I(x_i,t)$ by the laser amplitude L(t) at each instant in time, and integrating over the exposure time. The reader may recognize this repetitive phase-shift/multiply operation used to obtain the interference intensity in space as a *periodic convolution* of a time-dependent intensity oscillation I(t) with the reversed laser drive signal L(-t), evaluated at $t = x/v_s$.

The same result can be derived mathematically by noting that the traveling fringes can be described as a function of time and space:

$$I(x,t) = f\left(t - \frac{x}{v_s}\right)$$

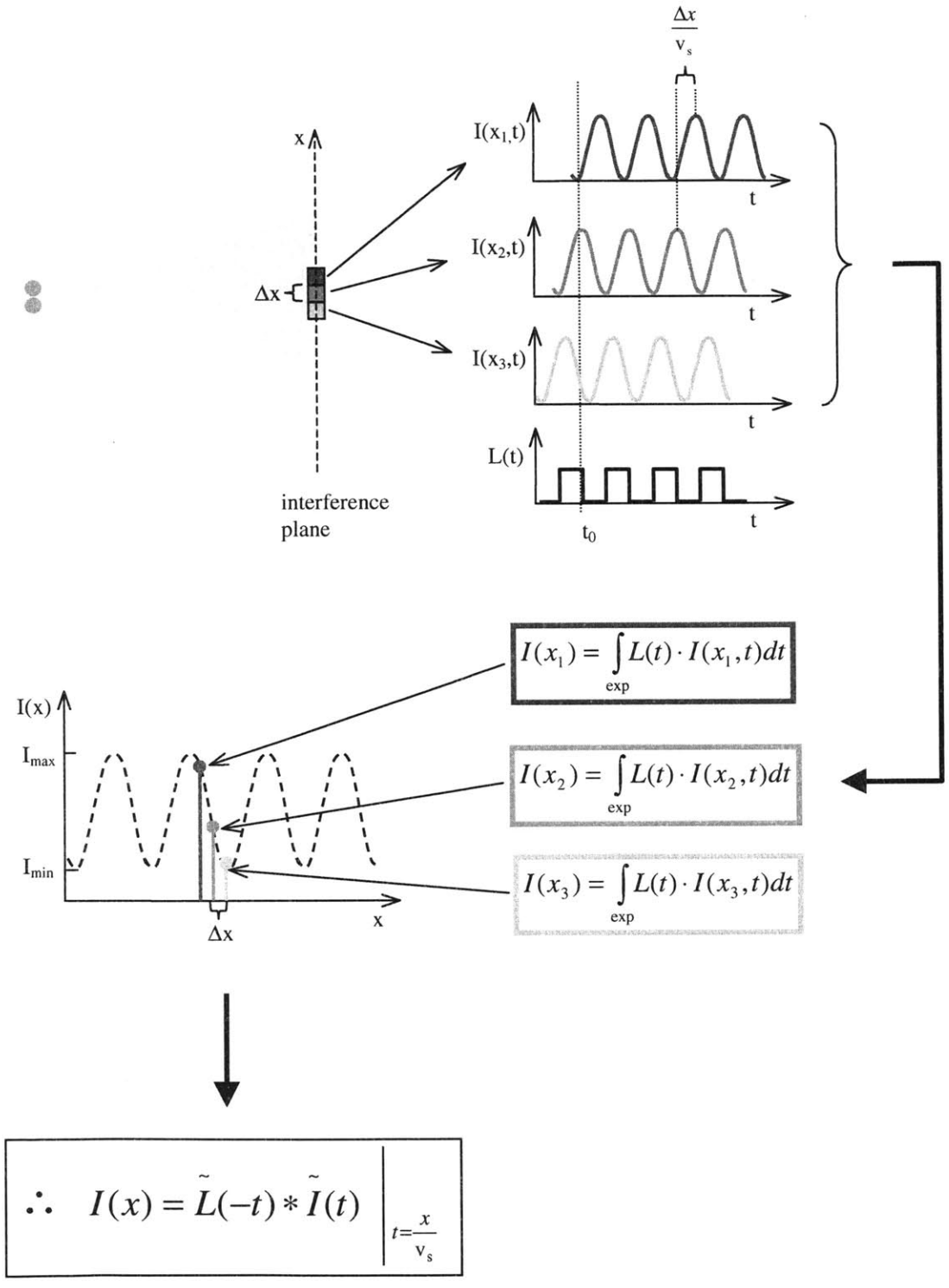

Figure 3.5 Using periodic convolution to model fringe intensity

As discussed above, intensity in space can be obtained by multiplying I(x,t) by L(t), and integrating over time:

$$I(x) = \int_{\text{exp}} L(t) \cdot f\left(t - \frac{x}{v_s}\right) \cdot dt$$

For an exposure time that is much longer than the least common multiple of the periods of the two waveforms, this is equivalent to periodic convolution:

$$I(x) = \tilde{L}(-t) * \tilde{I}(t) \Big|_{t=\frac{x}{v_s}}$$

From the above discussion it is evident that independent of the light intensity modulation, the fringe pattern I(x) must be a superposition of identical raised sinusoids that are phase-shifted in space relative to each other, and thus must be itself be a raised sinusoid with the spatial frequency determined by the source-point separation. To simulate the effect of various laser drive waveforms on the *contrast* of these stationary fringes, we can approximate I(x) by discretizing L(t) and I(t) and performing *circular convolution* on an integer number of cycles of the two waveforms. Since circular convolution corresponds to multiplication in the Discrete Fourier Transform domain, it can be approximated in Matlab (or any other signal processing tool) by taking the inverse FFT of the product of FFT's of the two signals. The following table compares the contrast and average intensity I (normalized by the CW laser output power I_{cw}) of the fringe patterns produced by several different laser drive waveforms, where we define as a measure of contrast the depth of modulation $M=(I_{max}-I_{min})/(I_{max}+I_{min})$.

Laser drive waveform (periodic with difference frequency)	**M**	**I/I_{cw}**
10% duty-cycle square wave	0.98	.11
50% duty-cycle square wave	0.63	.50
sinusoid	0.50	.50

When choosing the waveform to drive the laser, one must consider the amount of available light that reaches the object, the reflection properties of the illuminated object, as well as the sensitivity and dynamic range of the detector. If the laser is much more powerful than necessary, strobing the laser with short pulses will produce nearly perfect contrast and still provide sufficient light to reach the saturation limit of the detector. If the light power comes at a cost, then the tradeoff between contrast and light intensity becomes a more difficult engineering decision. It's important to note that this tradeoff is highly nonlinear. Halving the duty cycle from 10% to 5%, for example, will throw away half of the laser power, but will hardly change the already excellent contrast. Furthermore, as illustrated by the sinusoid results, some waveforms are preferable to others with respect to both contrast and light power. In fact, among waveforms that produce the same average light output, the square wave offers the best performance since it is the most compact in the time domain, resulting in the least variation in the phases of the superimposed sinusoids that make up the stationary fringe pattern.

The above analysis applies to CW (or continuous-wave) lasers. A variety of pulsed lasers exist, which concentrate all of their energy into periodic pulses that are much shorter than the period of the traveling interference pattern (e.g. <<25ns). If such a laser can be pulsed at the difference frequency of the interfering beams, fringes with nearly perfect contrast can be generated with no loss in the laser's output power.

3.3 An implementation of an acousto-optic projector

In the previous section we have seen how to generate a stationary interference fringe pattern and precisely and rapidly control it's spatial phase, spatial frequency, and intensity without a single moving element[3] using an electronic signal.

This chapter addresses some of the issues associated with implementing a prototype of such a high-speed solid-state acousto-optic projector.

3.3.1 Target Application

Design decisions for an AFI projector depend on tradeoffs between the range and extent of objects to be imaged, the desired resolution, and the imaging rate required. Since our primary objective is to demonstrate the concept of a high-speed AFI projector and to show that it can be applied to high-speed 3D imaging, a target application that would benefit from high acquisition speed but does not require high resolution or a large area of coverage is desirable.

One such application is 3D imaging of lip motion during speech. A 3D video of moving lips would be useful for generating models for speech analysis, lip reading, and voice recognition applications. Lips would also be a good target for the first prototype of the AOM AFI projector for the following reasons:

- The resolution requirements are minimal for modeling the shape of lips. Since lips have a smooth curved surface, resolution on the order of 1mm would be sufficient to sample the overall shape. Resolution is in part a function of the density of fringes

[3] Technically, the oscillating piezo-electric transducer inside the AOM is expanding and contracting at ~100MHz. This component, however, is very robust in its frequency response.

projected on the object (and hence the maximum source-point separation achievable with the AOM), and in part a function of the resolution and dynamic range of the CCD detector. A few dozen fringes across the lips should be more than sufficient. As will be seen shortly, this can be achieved with a variety of AOMs and can be well resolved with many high-speed CCD cameras.

- The extent of the lips is limited and they can be imaged at close range. As a result, projector power output of only a few milliwatts should be sufficient to illuminate the lips a few feet away, even for very short exposure times and low sensitivity characteristic of high frame-rate CCD cameras. Such power levels are available in a number of inexpensive diode lasers, and are considered eye-safe even a few inches away from the projector.
- The shape of the lips is smooth, simplifying the phase unwrapping steps in the AFI process.
- Lips are not prone to specular reflection and can be easily coated with white powder to improve their reflectivity properties.

3.3.2 System design

Figure 3.6 shows a block diagram of a prototype acousto-optic AFI projector that was built and tested in the laboratory. A photograph of the actual setup is shown in Figure 3.7. The following subsections address design considerations for each system component:

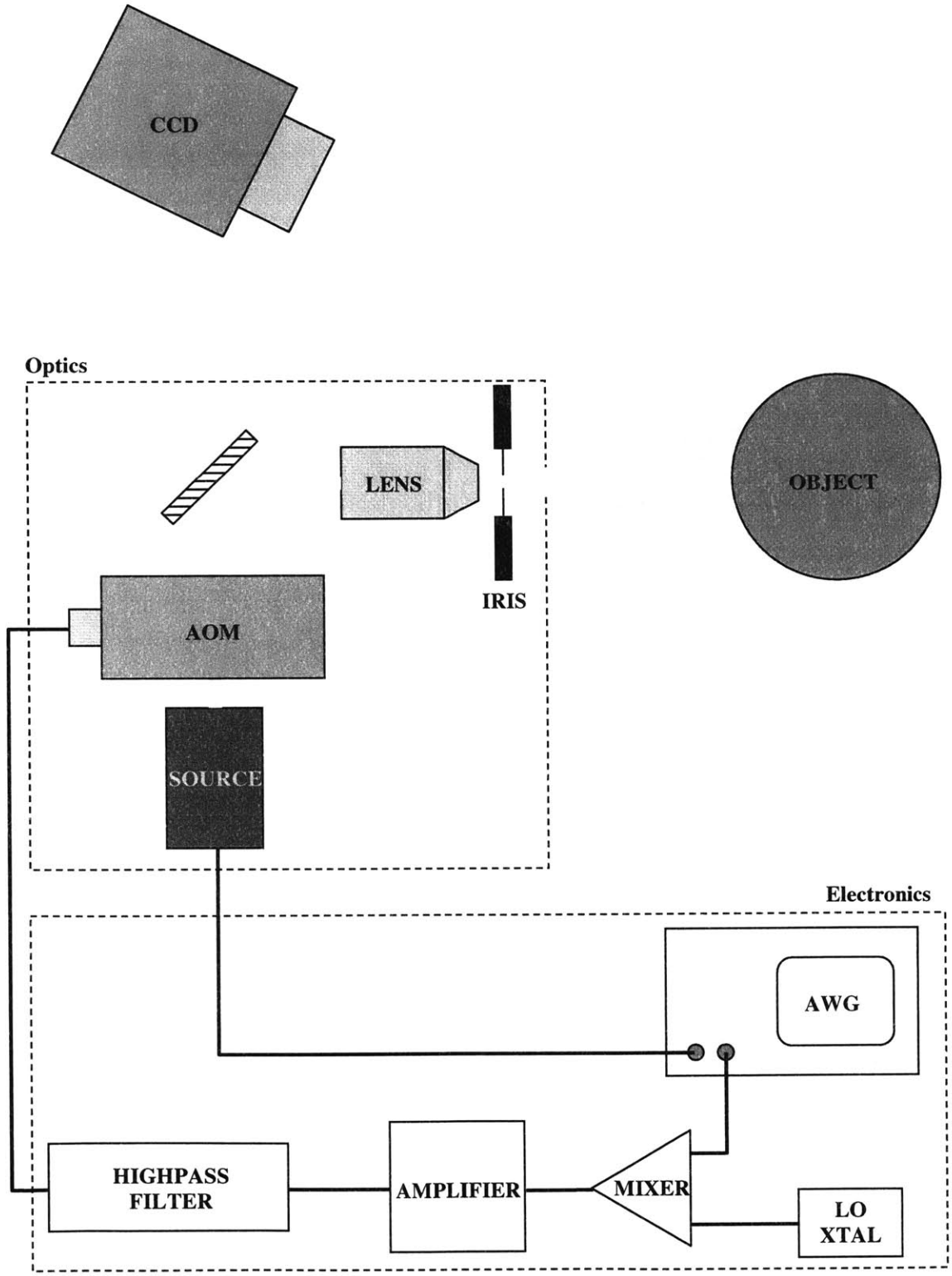

Figure 3.6 Elements of laboratory acousto-optic AFI setup

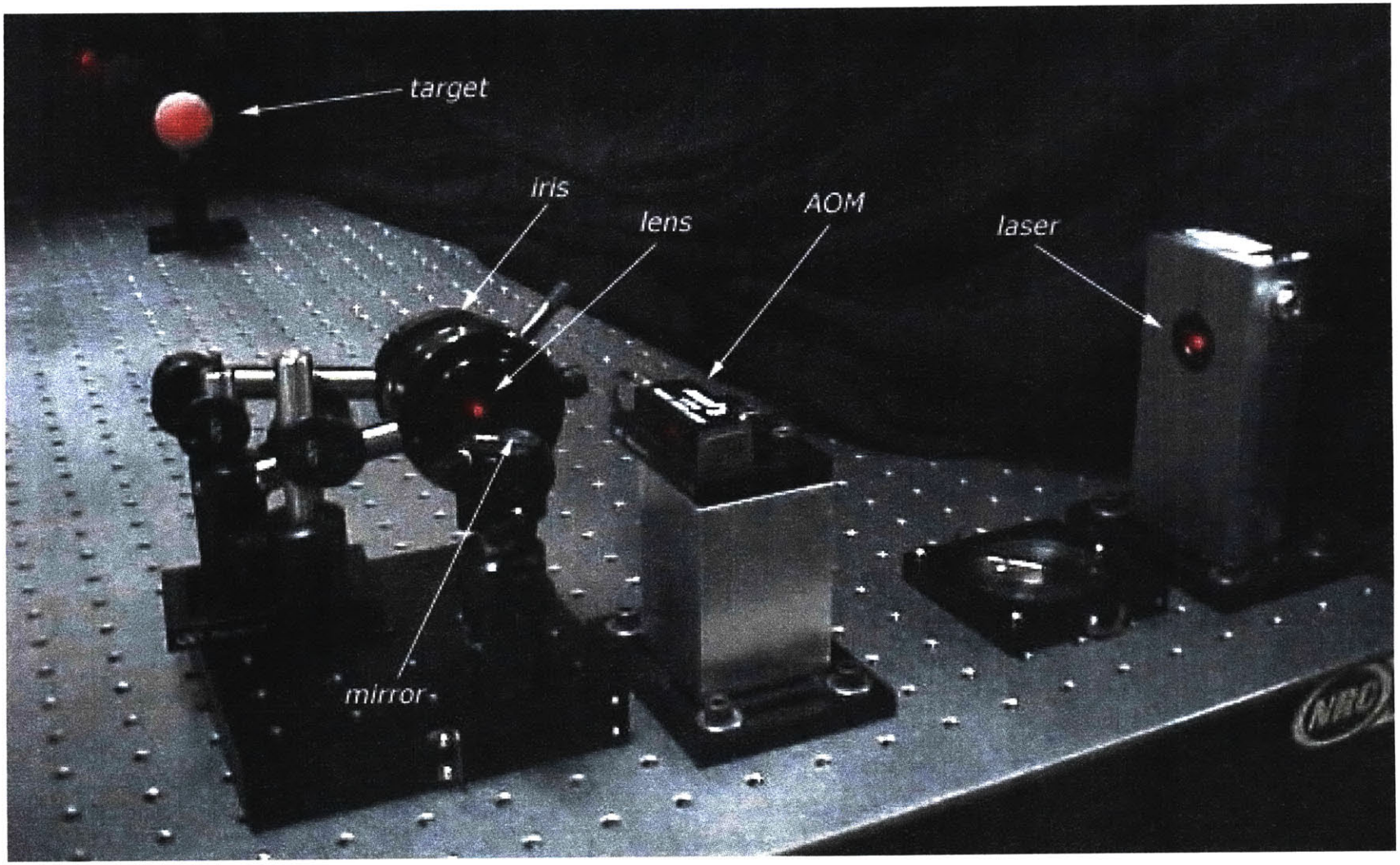

Figure 3.7 Acousto-Optic AFI Setup

Source of coherent radiation

Choosing an illumination source involves weighing of several parameters: power, wavelength, modulation bandwidth, coherence length, and of course cost. Since the object proximity is on the scale of a few feet for this prototype, it turns out that a 20mW laser would be sufficient to illuminate most objects. The common diode laser seems like a natural choice for providing this kind of power output. Not only are diodes of this power range commonly available, but they are much less expensive than other CW laser technologies of comparable output power. In addition, unlike most other lasers, many diode lasers can be modulated at rates in excess of 50 MHz -- sufficiently rapidly to be able to generate a high-contrast stationary interference pattern -- without the need for an external amplitude modulator. Some pulsed diode lasers are even available.

On the other hand, diode lasers typically cover longer wavelengths from red to infrared. One would expect that a green or blue laser would produce finer fringes, resulting in better resolution. In fact, this is not the case due to the physics of the AOM. As the reader may recall, the angular separation between the diffracted beams, and hence the point-source separation, is directly proportional to the optical wavelength. The spatial frequency of interference fringes, on the other hand, is directly proportional to point-source separation, and *inversely* proportional to the optical wavelength. As a result, *there is no net dependence of the fringe spacing on the optical wavelength*! This can be understood intuitively from conservation of momentum. Since photons with longer wavelengths have less momentum than photons with shorter wavelength (momentum = $\hbar * 2\pi/\lambda$), they are deflected by a proportionately larger angle by the oncoming sound wave [4]. Thus, the appropriate course is to choose a wavelength near the optimum CCD

response. Not by accident, most CCD spectral response curves happen to coincide well with the commonly available red and infrared diode lasers.

One disadvantage of laser diodes compared to HeNe lasers, for example, is a very short coherence length: a few millimeters or less. Although this may not be enough in a projector with several widely-separated optical paths, in the AOM projector both beams share the same optical path and the coherence length required for high-contrast fringes is simply the greatest accumulated path difference at the interference plane -- i.e. the number of fringes in the interference pattern multiplied by the optical wavelength. For this prototype, for example, the required coherence length is only ~20μm. This is almost achievable with some LED's!

The laser chosen for this system is a Power Technology PMT series module with a 685nm 40mW diode laser. This very economical laser module is equipped with a TTL trigger input, making it trivial to interface and synchronize with the RF electronics that generate the AOM drive signal, and can be modulated at over 100MHz. While this is sufficient to obtain stationary fringes over the entire AOM bandwidth, the ~5ns step response does not allow duty cycles below ~30% with a difference frequency of 40 MHz, for example, thereby somewhat limiting the contrast at the largest point-source separations. A laser with an even faster modulation capability would be desirable to obtain high-contrast interference with higher bandwidth AOM's and even greater fringe densities.

Detector

Since the speed of the system is limited by the frame rate of the detector used, choosing a high-speed CCD camera is essential. However, as the exposure time is reduced, a stronger laser source is required to sufficiently illuminate the object. In addition, due to the short readout time, pixel count, bit depth, well depth, and signal-to-noise ratio of the CCD are in general sacrificed.

In this case the 8-bit 256x256 Dalsa MotionVision CA-D7 area scan CCD camera was used with a Nikon 60mm 1:2.8D AF Micro Nikkor lens. Although this camera is capable of rates of up to 955 frames per second, it was used at only a fraction of this speed (90 fps) due to the available software and the capture speed of the frame grabber at hand. As simulations have shown, the AFI technique is fairly insensitive to quantization noise, and even four-bit signal quantization is more than enough to achieve the desired resolution for the target application. Also, because of the low resolution requirements, a 256x256 CCD array provides a good sampling of the fringe pattern. Furthermore, even with the lens partially stopped to increase the depth of focus, a few milliwatts of output from the projector is enough to saturate the 11-ms exposures of the CCD because of the proximity of the target in this case. Nevertheless, CCD speed-vs.-performance tradeoffs must be carefully considered for more demanding applications.

AOM

There are many kinds of AOM's available, geared towards different applications, different wavelengths, as well as different performance requirements[4]. Listed below are some important characteristics to look for when choosing an AOM for an interference fringe projector.

- *Interaction Material* is the crystal material carrying the acoustic wave. Commonly used materials are dense flint glass, $PbMoO_4$, TeO_2, germanium, and quartz. Each material has unique optical and acoustic properties. TeO_2, for example, has the slowest acoustic velocity (0.617mm/μs) [14] and hence is used to achieve large deflection angles and high modulation rates. Quartz, on the other hand, transmits well in the UV range, while germanium is used mainly for far-infrared applications. $PbMoO_4$, which is the most commonly used material, has a relatively slow acoustic velocity (3.63mm/μs) and is insensitive to laser polarization. Most of the AOM models are available in several broad antireflection coating ranges.
- *Center Frequency* corresponds to the frequency of the drive signal that would meet the Bragg condition when the input to the AOM is aligned at the Bragg angle.

$$f_c = \frac{2 \cdot n \cdot \sin \theta_B \cdot v_s}{\lambda}$$

  As the Bragg condition dictates, the higher the center frequency the larger the Bragg angle for a given interaction material and a given optical wavelength, and hence the larger the separation between the first-order and the zeroth-order beams. Thus, a large center frequency would be desirable for a single-frequency drive AOM

[4] Currently the major suppliers are Isomet and IntraAction Corp.

projector discussed earlier. Note that as the typical center frequencies range from 40MHz to 300MHz, it becomes increasingly challenging to synthesize and power the AOM drive signal.

- *RF bandwidth* refers to the range of drive frequencies corresponding to the range of diffraction angles (a.k.a. scan angle) over which the first-order beam remains within 3dB of its intensity at the Bragg angle. This bandwidth, and the corresponding scan angle, varies as a function of the optical wavelength, center frequency, and the acousto-optic interaction length [17]:

$$\Delta f \approx 1.8 \cdot \frac{n \cdot \mathrm{v}_s^2}{\lambda \cdot f_c \cdot L} = 1.8 \cdot \frac{\mathrm{v}_s}{2 \cdot \sin(\theta_B) \cdot L}$$

Note that the RF bandwidth is wavelength-independent, and that it falls as the center frequency increases, unless of course the interaction length L is adjusted to compensate. In the case of the compound drive AOM projector, the largest possible Δf is preferable (regardless of the center frequency) since it results in the largest separation between the first-order beams, and hence the finest fringes. One must also take into account the modulation bandwidth of the laser, since for the largest point-source separation it will have to be amplitude-modulated near Δf to achieve a reasonable contrast in the fringe pattern.

- *Diffraction Efficiency* is the ratio of the intensity in the diffracted beam(s) to the intensity of the original beam, and is a function of the properties of the material, of the interaction length, and of the strength of the acoustic signal [14]:

$$\frac{I_{diffracted}}{I_{incident}} = \left(\sin^2 (1.4 \frac{0.6328}{\lambda \cdot \mu m} \cdot L * \sqrt{M_w I_{acoustic}} \right)$$

where M_w is a material-dependent figure of merit. Evidently, diffraction efficiency can be increased by supplying more power to the AOM, and values above 50% can by typically reached. While the highest possible diffraction efficiency is desired for the compound-drive projector, a 50% diffraction efficiency would be ideal for the single frequency drive projector that uses the first and zeroth-order beams to generate a fringe pattern.

- *Active aperture* is the maximum diameter of the laser beam that will fully interact with the traveling acoustic wave. An elliptical aperture is preferable for use with a diode laser, since the output of most diode lasers has an elliptical crossection.
- *Resolution* is characterized by the number of resolvable beams (a.k.a. "spots")[5], also known as the $\tau\Delta f$ product, where τ is the time required for the sound to cross the diameter of the optical beam. As expected, resolution is inversely related to the well-known divergence ratio, λ/D. Thus, AOMs with larger active apertures produce more resolvable spots and tend to be used as deflectors. *Note that AOM resolution is irrelevant for the AFI projector.* Because the laser beams have a Gaussian intensity distribution, they expand in a hyperbolic fashion as they propagate [14], and thus do not have to be resolved in the Rayleigh sense to generate an interference pattern. This is illustrated in Figure 3.8. In fact, it is possible to generate almost arbitrarily large fringes using the AOM technique simply by driving the AOM with a compound signal with a very small difference frequency.
- *Rise time* is the time for the diffracted laser beam intensity to rise from 10% to 90% of its maximum value in response to a step in the amplitude of the acoustic wave, and

[5] A "resolvable spot" is defined by the Rayleigh criterion (see Hecht p371)

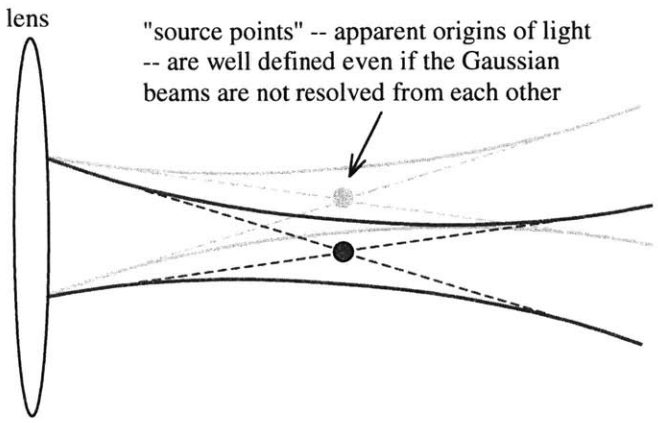

Figure 3.8 Gaussian Beam Propagation

determines the modulation bandwidth of the AOM. Since the entire aperture must be filled with the new acoustic level before the diffracted beam fully responds, the rise time is proportional to the ratio of the aperture size and the acoustic velocity. Thus, while AOMs with a large active aperture are good beam deflectors, they are slow beam intensity modulators. Rapid beam intensity modulation is not generally important for an interference pattern projector. However, since rise-time is closely related to the frequency and phase modulation bandwidth, it may be an important consideration for interference pattern projection applications where high-bandwidth active drift compensation is important.

- *Power requirements* for achieving optimum diffraction efficiency depend on the material used, the optical wavelength, as well as on the acousto-optic interaction length, as the diffraction efficiency equation indicates. One or two Watts of drive power are typically sufficient for red and infra-red wavelengths. Significantly overdriving the AOM would actually result in loss of diffraction efficiency and eventually possible damage to piezo-electric transducer and internal power-matching electronics.

With the above considerations as well as cost and size in mind, Isomet's 1205-C2-804 AOM coated for the operational wavelength of 685nm was used for this prototype. This device is only 22 x 16 x 51 mm^3 in size, has a center frequency of 80MHz, and has an RF bandwidth of 40MHz, corresponding to a maximum angular separation of ~0.6° between the two first-order beams in a compound drive projector. It has a 2mm x 6mm oval

aperture suited for the laser diode's beam crossection, and requires ~1.5W of RF power to achieve ~85% diffraction efficiency.

RF electronics

One of the key strengths of an AOM projector is that most of the complexity is shifted from mechanical and optical hardware to electronics. In particular, all parameters of the fringe pattern are controlled with a single compound RF (radio-frequency) drive signal to the AOM, which is a superposition of two sinusoids of independently controlled frequency, phase, and amplitude.

One approach to generating such a sinusoid is to use a voltage-controlled oscillator (VCO). Although VCOs are readily available for RF frequencies, it is rare to find one that is linear and jitter-free over the complete bandwidth required – in this case, from DC to 20MHz. Furthermore, in order to adjust the phase of the sinusoid, the VCO must be placed in a phase-locked feedback loop. Such circuits are prone to phase jitter, noise, and unwanted oscillations, and hence are difficult to design well, especially for such a large bandwidth.

In the author's opinion, however, the simplest, most robust, and most flexible means of generating the AOM drive signal is digital synthesis. This can be done very inexpensively using several small Direct Digital Synthesis VLSI chips. Using a 32-bit counter, some onboard sine and cosine ROM, and a 12-bit DAC, these chips can generate quantized sinusoids with frequencies ranging from a fraction of a Hertz up to 40 MHz with 32-bit precision over phase and frequency control! Alternatively, as was done in the case of this prototype, an arbitrary waveform generator such as the Sony/Tektronix

AWG2010 can be used to synthesize the AOM drive waveforms. The AWG2010 also uses DDS technology, but can be programmed to synthesize a good approximation to *any* desired waveform up to approximately 50MHz in bandwidth using a 250MHz sampling clock. A model with a 1GHz sampling clock is also currently available. Although the AWG2010 is an expensive device, it was available for use and offers immense flexibility for experimenting with supplying different waveforms to the AOM. By writing a simple script on a computer and downloading it to the AWG, it was possible to generate compound waveforms for projecting interference fringe patterns with a variety of spatial frequencies and phase shifts. In addition, the AWG offers several TTL "marker" outputs which are ideal for synchronously pulsing the laser at the difference frequency with a desired duty cycle.

Because DDS produces a sampled and quantized waveform, artifacts corresponding to harmonics of the desired frequency appear in the spectrum of the signal. These are more problematic for low-frequency signals, since they occur closer to the frequency of interest. The harmonics are much lower in amplitude than the main signal, but they can be amplified by nonlinear magnitude response in the frequency multiplier and can cause faint beams at the output of the AOM. Although this is a minor effect, it can be removed by constructing a variable-frequency band-pass filter to isolate the frequencies of interest and/or by carefully selecting a good RF multiplier with linear behavior over the desired frequency and power range.

Choosing a multiplier is one of the more important decisions in the electronics design, since it is prone to introduce or amplify noise in the signal. For this prototype, the Mini-Circuits Level 17 ZP-3H balanced RF frequency mixer was used to multiply

the compound waveform by a carrier frequency. Mixers use passive components such as diodes and inductors to multiply a weak RF signal by a stronger Local Oscillator (LO) signal. They are inexpensive and are available for various bandwidths as well as input power ranges. However, depending on the frequencies and power levels used, mixers can exhibit nonlinearities including leakage of LO signal into the output, introduction of 3^{rd}-order harmonic distortions, and amplification of existing harmonics relative to the desired frequency. Absolute LO power level, relative power levels of the LO and RF signals, and the frequency of operation should be optimized against the conversion loss, isolation, and 3^{rd}-order intermodulation distortion curves of the particular mixer model to minimize ghost beams such as have been seen with mixers used in the course of this work.

Alternatively, an active analog multiplier IC such as the Analog Devices AD835 can be used to multiply the signals. Unlike the mixer, which is packaged as a small box with three SMA terminals, this chip requires some external wiring, but it offers very good linearity and accuracy over a 200MHz bandwidth. Latest experiments are showing it to be a big improvement over the performance of the mixers.

In order to bring the power level up to the ~2 Watts required for best AOM diffraction efficiency, the Mini-Circuits ZHL-1000-3W amplifier was used. This amplifier can handle over 3 Watts of power, has a fixed gain of at least 38dB, and is somewhat of an overkill for this application. Finally, a custom-made 11-pole elliptical highpass filter was used between the amplifier and the AOM to cut off low-frequency artifacts.

Optics

The optical design of this prototype consists of choosing a lens. A Nikon 4x 0.1NA microscope objective was chosen in this case to achieve a good coverage of the object: a ~10° half-angle measured along the major axis of the elliptical light cone. Because microscope objectives are designed to have a distant back-focal plane, they are ideal for focusing a coherent laser beam. On the other hand, an AR-coated plano-convex lens with a 10mm focal length would probably have worked just as well, and possibly better since the microscope objective was not coated specifically for 685 nm.

Note that there is an important tradeoff between fringe density and beam divergence to consider when choosing the focal length of the lens. The source point separation due to a given difference frequency in the AOM drive signal, and hence the resulting fringe density, is a function of the focal length of the lens. For a thin lens, this dependence can be approximated as:

$$a \approx \mathrm{f} \cdot \tan(\Delta\theta) \approx \mathrm{f} \cdot \frac{\lambda \cdot \Delta f_s}{n \cdot \mathrm{v}_s}$$

where f is the focal length of the lens, and a is the point source separation, and $\Delta\theta$ is the angular separation between the interfering beams. Although increasing the focal length results in a larger a and a finer fringe spacing, it also reduces the divergence of the interfering beams. In fact, the total number of *visible* fringes is always the same.

As shown in the diagram, an iris was placed at the focal plane to block the zeroth-order beam from interfering with the first-order beams. A more comprehensive solution would be to make a spatial filter mask by placing a thin metal plate at the focal plane and drilling minute apertures at locations corresponding to the desired source-point

separations. In addition to blocking the zeroth-order beam as well as any ghost beams generated by harmonics in the AOM drive signal, it would also serve to remove most distortions present in each beam and the associated background noise in the interference pattern by filtering out everything except the central Gaussian lobe in the beam's focal plane diffraction pattern.

3.3.3 Results

The complete system is capable of projecting over twenty interference fringes with a 40MHz difference frequency driving the AOM. This is more than sufficient to demonstrate the concept of a solid-state projector and to be able to create surface maps of some interesting objects.

Figure 3.9 shows a golf ball illuminated by interference fringes produced with the acousto-optic projector. In this case 30MHz difference frequency was used to drive the AOM, and a 25% duty cycle square wave was used to pulse the laser. The fringes exhibit good contrast, as would be expected from a 90% modulation depth predicted by simulations.

The golf ball was coated with white spray paint to eliminate specular reflections from some patches of the glossy surface. Depending on the chosen exposure time, such anomalies lead to either saturation of the CCD in those areas, or to reduced sensitivity in the areas that do not produce specular reflection. This kind of abrupt intensity variation will be true of many potential targets with varying textures and surface angles. While coating the object with diffuse paint can be an effective approach, paint not only hides the finer features on the object's surface, but usually destroys the object -- an outcome that is

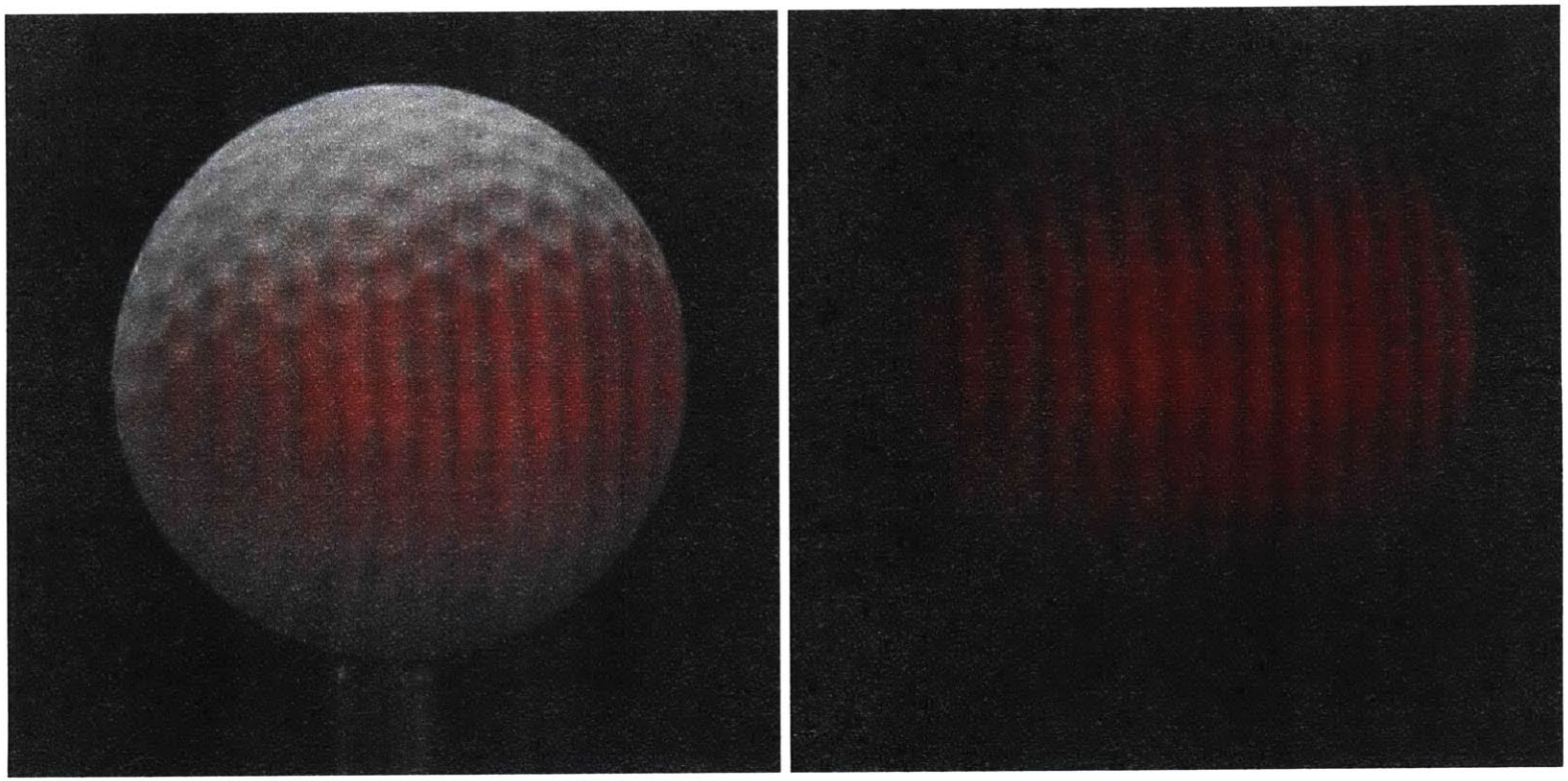

Figure 3.9 Results: 30MHz fringes on a spray-painted golf ball

often not desirable. Another way of using the CCD's dynamic range efficiently for all regions of the object without coating it is to take a succession of exposures at different interference fringe intensities. By using the dimmer fringes to reconstruct the bright surface patches and using the brighter fringes to reconstruct the more diffuse areas, the complete surface map can be obtained[6]. For stationary objects, the high frame rate of an AOM-based AFI system allows taking a rapid progression of exposures at a wide range of fringe intensities, enabling the reconstruction of all illuminated surfaces for a generic object with unknown surface reflectance properties.

Also visible in Figure 3.9 is slight background intensity structure in the interference pattern due to intensity variations in the laser beam (dirt on the optics would produce much more conspicuous circular diffraction patterns). Although one of the benefits of the AFI technique is that phase measurements are minimally affected by such spatial intensity variations in the laser beam, these local brightness variations do act to slightly reduce the dynamic range available in some areas of the object. A more pronounced setback is dealt to the visual appeal of the interference pattern. As mentioned before, however, placing a spatial filter mask at the focal plane of the focusing lens can among other things greatly improve the appearance of the fringes.

Although the AOM used in this experiment is capable of projecting only about two dozen fringes, fringe density can be greatly increased for more demanding applications by using an AOM with a greater RF bandwidth, or by interfering the first-order diffracted beam with the zeroth-order beam and using a single frequency to generate the acoustic wave. Used in this fashion, the Isomet LS55 AOM, for example,

[6] The saturated pixels may "bleed" into neighboring pixels, reducing the effectiveness of this approach near saturated regions. Many CCD's, however, have anti-blooming gates that greatly reduce this effect.

can produce nearly 400 fringes -- far more than can be taken advantage of by most scientific CCD cameras. Even higher angles of deflection can be obtained through "beam steering" [17]. This technique relies on a serially-stacked phased array of piezo-electric transducers along the acousto-optic crystal to "steer" the beam further and further from the Bragg angle. Although more costly to implement, this approach can potentially be used to generate thousands of fringes.

3.4 Benefits of the acousto-optic projector

The acousto-optic projector has few inherent limitations. Even though the number of projected fringes is limited by the deflection range of the AOM, hundreds or thousands of fringes can be generated if necessary using the beam steering approach mentioned above. Another issue is the loss of laser power due to amplitude modulation of the laser beam necessary to freeze the traveling fringes. However, even with 50% modulation, high contrast fringes can be obtained[7]. On the other hand, the acousto-optic projector has many benefits to offer for projecting interference patterns in general and for Accordion Fringe Interferometry in particular:

- *Robustness:* The acousto-optic projector consists of only four elements: a laser, an AOM, a lens, and RF electronics. It is not difficult to fathom the ruggedness and reliability of the solid-state optical and electronic components. The AOM itself is also very robust. Acousto-Optic Modulators are used for modulating laser intensity, scanning laser beams, and frequency filtering in a variety of applications and can

[7] It may be possible to generate and control stationary fringes without the need to modulate the laser beam by inducing standing waves in the acousto-optic crystal. This approach is yet to be explored.

handle a range of optical powers up to 200W. High quality laser printers, optical signal processing, spectroscopy, and rangefinding are just some of the industrial and military applications that rely on AOMs. As a result, AOMs are made to be very dependable and suitable for use in adverse environments. By contrast, high vibration, temperature drifts, and large gravitational forces would pose insurmountable obstacles for a projector system that relies on moving components.

- *Accuracy and Repeatability:* Given a stable environment, the resolution in the spatial phase and frequency of the projected interference pattern is dependent largely on the precision of the electronics and the optical quality of the collimating and focusing lenses. With a 32-bit resolution in the frequency and phase of the digitally-synthesized electronic signal, frequency steps of a few millihertz, and phase shifts of a few nanodegrees can be made repeatedly! This kind of performance can not be matched by a system that relies on moving components, where frequency and phase uncertainties are a significant source of error in data processing. Of course, temperature drifts can result in mode-hopping of the laser, as well as distortions in the optical path of the laser beam. This kind of behavior, however, will affect any optical system that relies on a laser, and well known environment control techniques can be used to mitigate the effects. In addition, due to the fast, complete, and precise control over the fringe pattern, active compensation for temperature drift may be effective with the acousto-optic projector.
- *Speed:* Modulation bandwidth of nearly 1MHz is more than is required for updating the fringe pattern at video rates. This large of response rate, however, can be utilized in a high-speed electronic feedback system interfacing the AOM drive electronics

with a series of sensors (e.g. accelerometers, photodetectors, temperature sensors) to allow active compensation for high-frequency vibrations and temperature fluctuations in the environment. In addition, the high modulation rate can be used to measure high-frequency vibrations in three dimensions – by matching the phase or frequency of the fringes with a lateral or range motion of a vibrating reference pattern, for example.

- *Arbitrarily large reference fringes:* Because of the very small source-point separation involved (e.g. 4μm), projecting large stable interference fringes can be a source of difficulty for an interference projector that relies on rearrangement of optical components to control fringe density. For a compound-drive AOM fringe projector, on the other hand, the spatial frequency of the fringe pattern is a function of the difference frequency in the AOM drive signal only, and as a result can be made almost arbitrarily small. Although the present AFI technique does not need to rely on large interference fringes for phase unwrapping, the capability of generating them offers another degree of flexibility in projecting an interference pattern in general.
- *Short coherence length:* Due to the shared optical path of the two interfering beams in the acousto-optic projector, the coherence length requirements are very relaxed – e.g. on the order of 20μm – allowing for a greater choice in sources of illumination.
- *Portability:* With a diode laser as the radiation source, at 22x16x51 mm^3, the AOM is the largest component in the optical path of the acousto-optic projector, fitting comfortably on the palm of a hand. AOM drive electronics using DDS VLSI technology and a custom-made amplifier can be made small enough for the entire device to occupy a volume the size of a person's fist (batteries not included).

- *Economy:* If a DDS VLSI strategy for the RF electronics is pursued, the cost of such a system today would be somewhat evenly distributed between the AOM, the diode laser, and the entire package of electronics, amounting to an estimated parts cost of $2000 for a single prototype, although for an application demanding more fringes, a more expensive AOM would be in order. Of course, the projector can be mass-produced at a fraction of this cost, resulting together with an economical CCD detector in a 3D imaging product affordable to the research community, and ultimately to the consumer.

Chapter 4

Depth-Retrieval For Stationary and Moving Targets

Although the main objective of this work was to design and implement a high-speed interference pattern projector, a basic algorithm for automatically extracting depth information via spatial phase estimation was also implemented in order to demonstrate the 3D imaging speed possible with an acousto-optic AFI system. The algorithm as well as the 3D reconstructions obtained with a prototype acousto-optic AFI system are discussed below.

4.1. Algorithm for depth retrieval using spatial phase estimation

4.1.1 Triangulation

As explained in Chapter 2, depth information about a reflective object can be obtained by projecting an interference fringe pattern onto the object followed by triangulation using a single detector. The triangulation model used for this algorithm is

depicted in Figure 4.1, where the two-beam interference fringe pattern is approximated by a raised cosine function [12]:

$$I = I_0 \cdot \cos^2\left(\frac{y \cdot a \cdot \pi}{s \cdot \lambda}\right) + I_{DC}$$

Note that I_0 and I_{DC} are taken to be constant since the AFI method is insensitive to cross-pixel variations in amplitude and offset of the fringe pattern, but is instead concerned with the argument of the cosine function. By applying some geometry (see Figure 4.1), it becomes clear that once the unwrapped argument, or spatial phase, of the raised cosine function is established, the distance from the detector to the point imaged by a given pixel can be derived. Note that because the triangulation relies solely on the characteristics of and spatial relationship between the projector and the detector, no information about the position or orientation of the object must be known apriori. Of course, erroneous measurements will result in regions cast in shadow by folds or corners of the object.

The key parameters necessary for this triangulation algorithm are: α, the angle between the null axis of the projector and the plane of the CCD; b, the baseline between the projection of the center of symmetry of the source points onto the CCD plane and the central pixel on the CCD; r, the distance from the CCD plane to the centroid of the point sources; δ, the half-angle of the field of view of the lens; and a, the point-source separation. Errors in these parameters have a global effect on all pixels and do not cause discontinuities in the surface reconstruction, so rough measurements in the laboratory are sufficient to obtain the overall, perhaps slightly distorted, shape of the object. Of course, once the configuration of the system is solidified, these parameters can be exactly

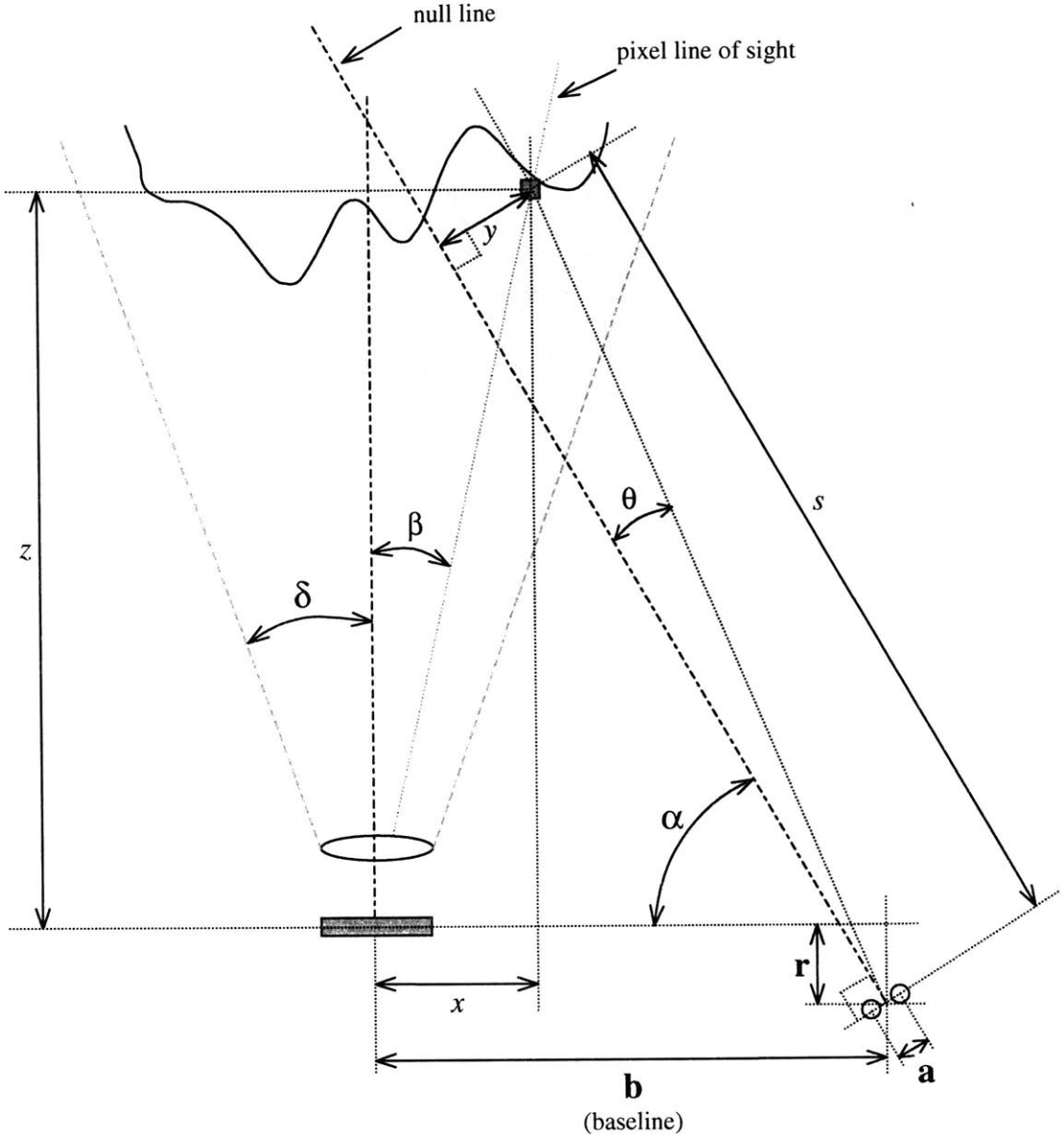

$$I = I_0 \cdot \cos^2\left(\frac{y \cdot a \cdot \pi}{s \cdot \lambda}\right) + I_{DC} = I_0 \cdot \cos^2\left(\phi_{unwrapped}\right) + I_{DC}$$

$$s = \frac{(z - y\cos\alpha + r)}{\sin\alpha} \quad \rightarrow \quad \frac{y}{s} = \frac{y\sin\alpha}{z + r - y\cos\alpha} = \frac{\lambda \cdot \phi_{unwrapped}}{a \cdot \pi} = \tan\theta$$

$$x = z \cdot \tan\beta \quad \rightarrow \quad y = [z + r - (b - x) \cdot \tan\alpha] \cdot \cos\alpha = z \cdot (\tan\beta \cdot \sin\alpha + \cos\alpha) - b \cdot \sin\alpha + r \cdot \cos\alpha$$

$$\therefore \quad z = \frac{r\tan\theta + (b\sin\alpha - r\cos\alpha) \cdot (\tan\theta \cdot \cos\alpha + \sin\alpha)}{(\tan\beta \cdot \sin\alpha + \cos\alpha) \cdot (\tan\theta \cdot \cos\alpha + \sin\alpha) - \tan\theta}$$

Figure 4.1 Triangulation

measured, and absolute depth measurements can be obtained for any object placed in the field of projected illumination.

4.1.2 Phase Unwrapping

Errors in the phase-map, on the other hand, will vary from pixel to pixel, causing noise and discontinuities in the reconstructed surface of the object. Thus it is the process of measuring and unwrapping the spatial phase for each pixel that is the main challenge in an AFI algorithm. The implemented phase unwrapping method is based on the Progressive Fringe Division algorithm developed by Shirley [1]. It relies on phase measurements taken at a progression of fringe spacings to unwrap the phase measurement taken at the smallest fringe spacing independently for each pixel. As explained in Chapter 2, at each point-source separation a in this progression, the phase at each pixel is computed to within a 360° ambiguity by imaging three fringe patterns phase-shifted relative to each other by 90°. Note that no matter what a is, the spatial coordinate of the pixel (triangulated from $\tan\theta$) must remain the same. Therefore, we can unwrap a phase measurement taken at a given point source separation a_1 by finding that integer fringe number n that results in a value of $(\tan\theta)_1$ that is nearest to $(\tan\theta)_2$ calculated using an unwrapped reference phase measurement taken at a smaller point source separation a_2. The entire process is illustrated in Figure 4.2 from the point of view of a single pixel and the pixel array as a whole.

The software written to implement this algorithm consists of several self-documenting Matlab modules, which are included in Appendix A. The surface reconstruction algorithm was tested for correctness using simulations in Matlab. A

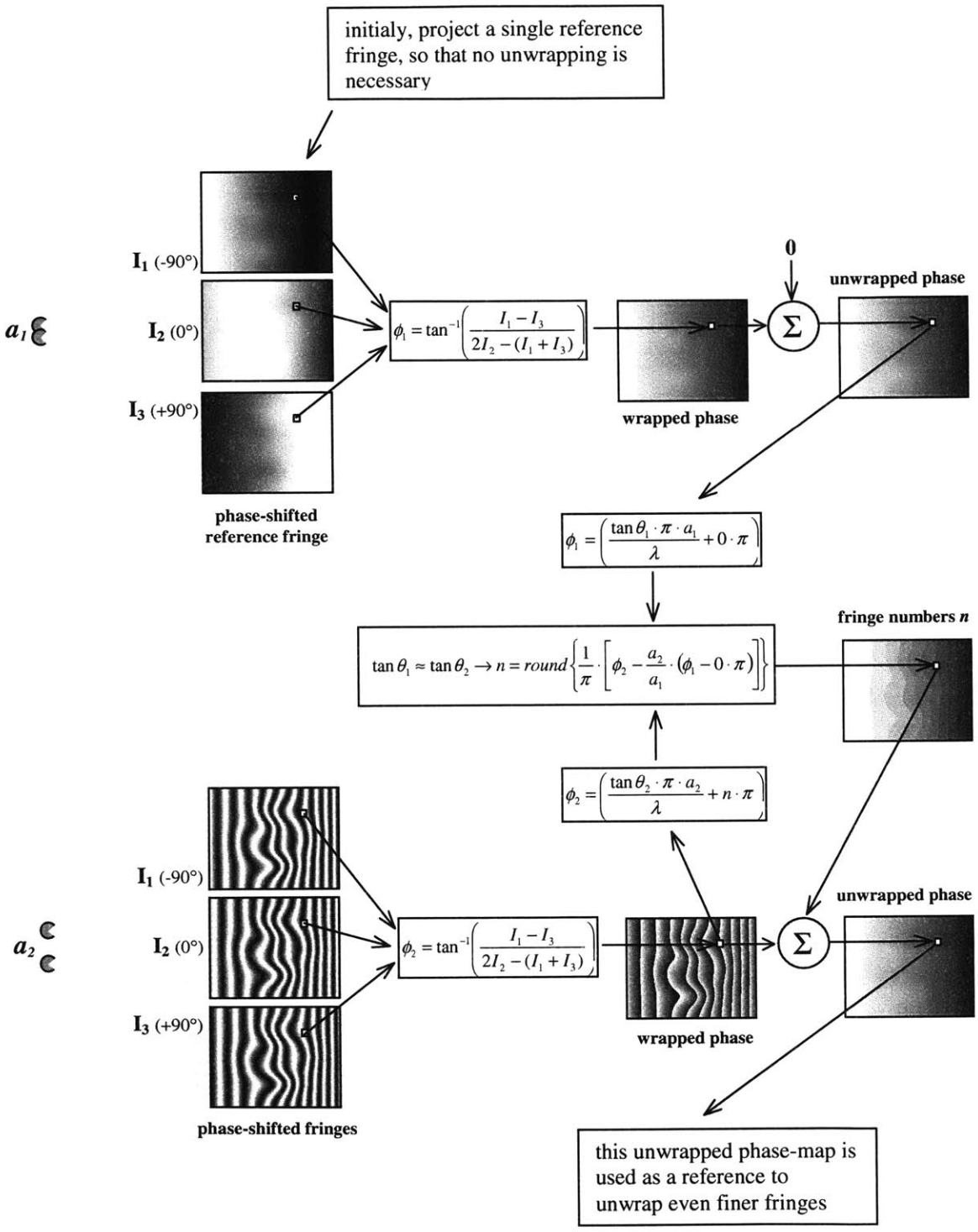

Figure 4.2 Phase unwrapping

surface was generated using the *peaks* function, and simulated fringe patterns of different densities were projected onto it using the raised-cosine model (without taking shadows into account). The algorithm outlined above was then used to reconstruct the 3D surface. As shown in Figure 4.3, the reconstructed surface is indistinguishable from the original *peaks* function. The same results were obtained with a variety of geometric system parameters used to simulate the fringes. The Matlab functions and scripts used to perform the simulations are also included in Appendix A.

4.2 Measurements and Results

To test the acousto-optic AFI system as a whole, a white spray-painted golf ball was used as a target. The golf ball was placed 56cm away from the focal plane of the projector, and the geometric parameters necessary for triangulation were measured to be: α=43°, b =370mm, r =-426mm, and δ=1.72°. Three fringe spacings used to unwrap the phase were generated using difference frequencies of 1,6, and 40MHz in the AOM drive signal, corresponding to source-point separations of 4.45, 26.7, and 178μm, respectively. A 50% duty cycle square wave was used to drive the laser in all three cases, resulting in a 66% modulation depth of the fringes. Figure 4.4 shows the three resulting fringe patterns, the corresponding wrapped phase-maps calculated using three 90° phase-shifts at each fringe separation, as well as the unwrapped phase-maps produced using the algorithm outlined above. All nine exposures were taken in 100 milliseconds with the 256x256 8-bit Dalsa CA-D7 CCD camera running at 90 frames per second.

The resulting surface map shown in Figure 4.5 demonstrates the feasibility of autonomous high-speed 3D imaging with an acousto-optic AFI system. In addition to the

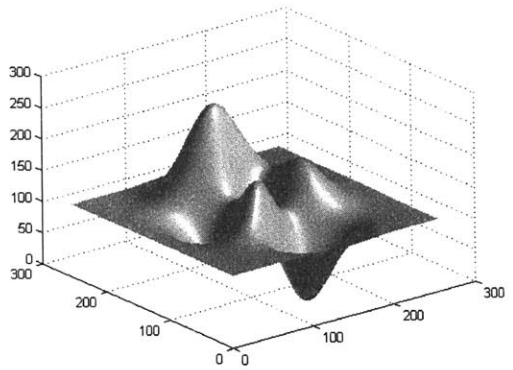

Simulated Surface

distance from source: 50cm
depth extent: 5 cm

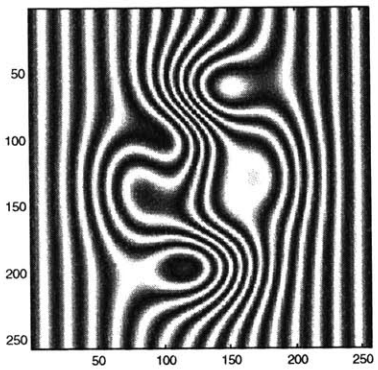

Simulated fringe projection

$\alpha = 43°$
b = 370mm
r = -426mm
$\delta = 1.7°$
$\lambda = 685nm$
a = 178μm

quantization: 256 levels

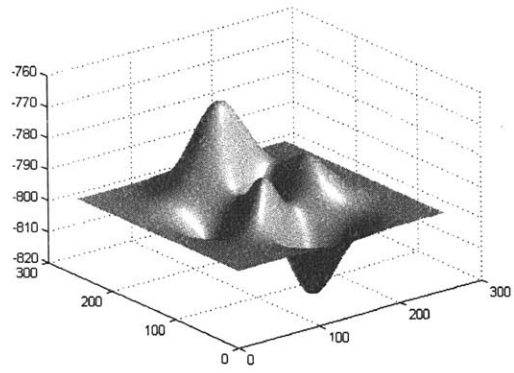

Reconstructed Surface

Figure 4.3 Simulations show algorithm correctness

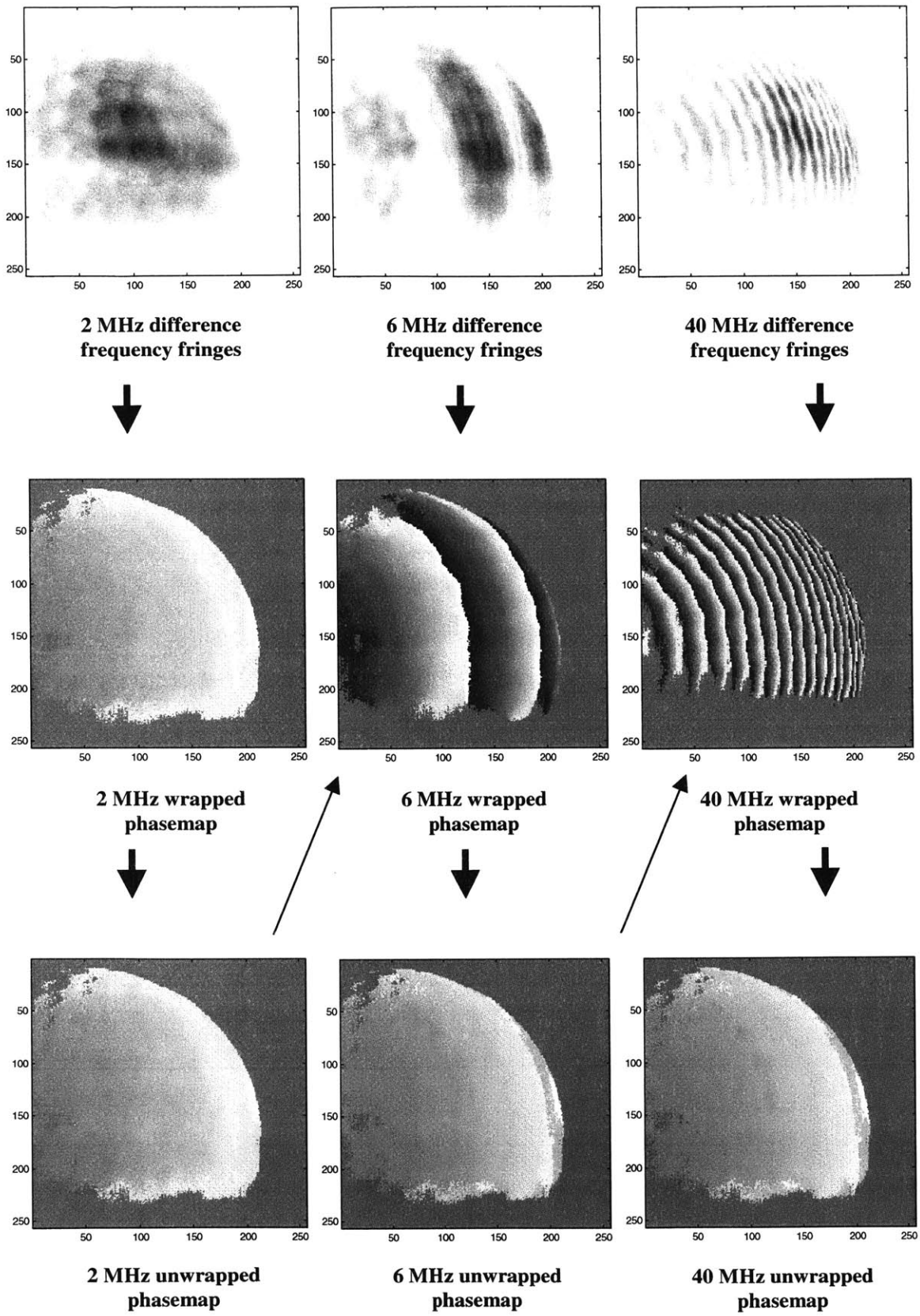

Figure 4.4 From Fringes To Phasemaps

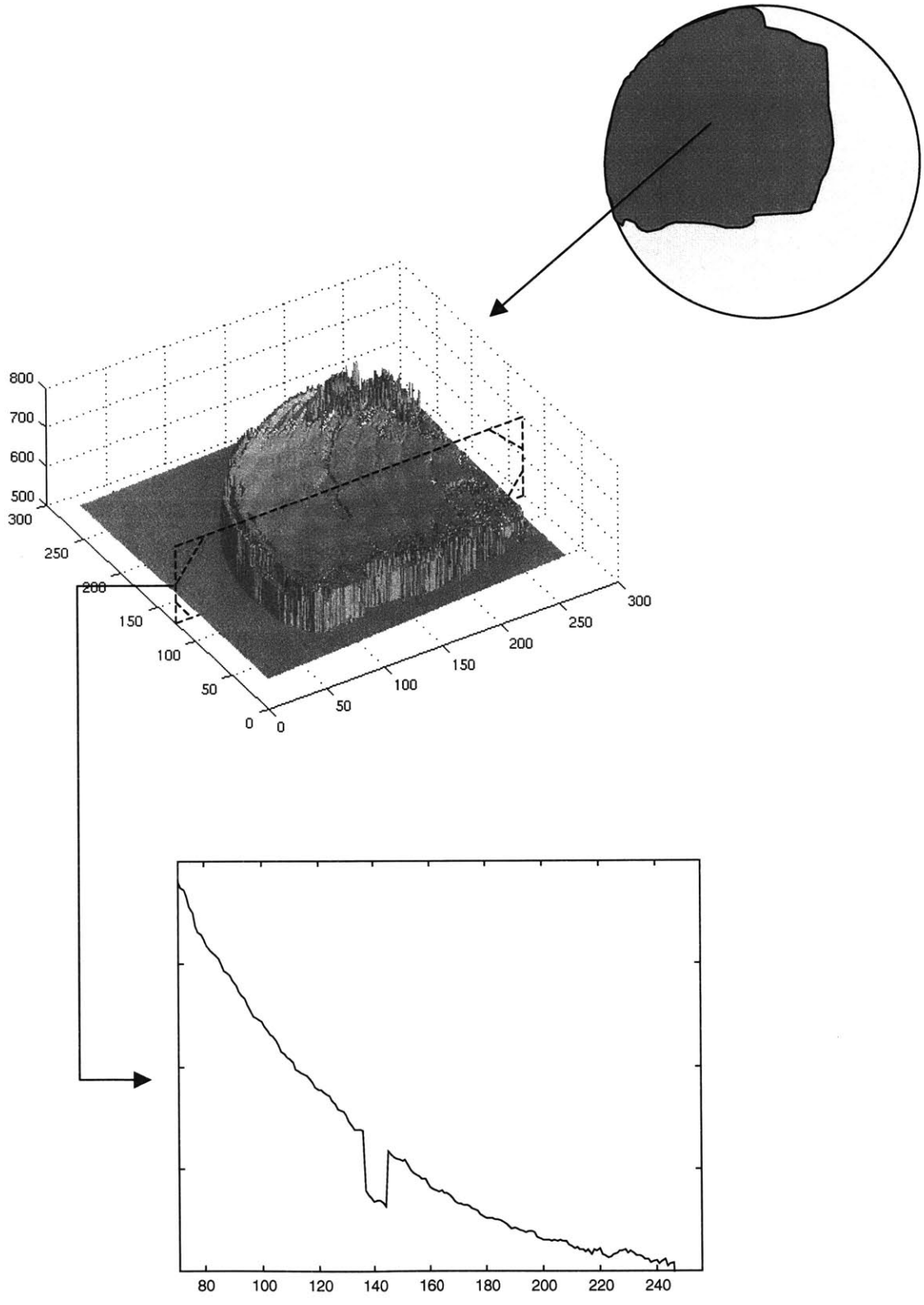

Figure 4.5 3D reconstruction of the illuminated surface of a golf ball

short data acquisition time, it took only ~4 seconds on a 166 MHz Pentium-class computer to reconstruct a surface from the collected data -- without significant optimizations in the Matlab code. This processing time is encouraging, since it suggests the possibility of real-time processing using a dedicated DSP board.

This first attempt at a 3D surface reconstruction using acousto-optic AFI not only shows the overall shape of the golf-ball, but also resolves sub-millimeter indentations in the golf ball. The errors in the surface map also reveal some issues to be considered when making 3D measurements using this system in the future.

For example, it is evident from the images in Figure 4.4 that the intensity of the reflected light is distributed very unevenly across the golf ball due to the varying orientation of the surface. While there is little that can be done about this for a quickly moving target, for a stationary object a series of nine-frame sequences of varying intensity could be taken to cover the entire surface of the golf ball with fringes as outlined in Chapter 3.

One may also notice that the fine background fringes are better focused than the larger foreground fringes. Badly focused fringes tend to smear phase measurements of neighboring pixels, ultimately resulting in a loss of depth resolution. If there is no shortage of light, a greater depth extent of the object can be brought into focus by increasing the laser intensity and stopping down the lens aperture to increase the depth of focus of the detector[8].

Also, evident in the surface reconstruction, are small-amplitude high-frequency ridges that are present throughout the surface and appear to trace the curvatures of the

[8] The size of imaged laser speckle tends to increase as the lens aperture is reduced. Since laser speckle is a source of noise in phase measurement, this tradeoff must also be considered.

interference fringes. The most likely cause of these irregularities is the presence of "ghost" beams due to harmonics in the electronic AOM drive signal. Since the phase of the faint low contrast fringes produced by the ghost beams correlates with the phase of the primary fringes, the ghost fringes would not be eliminated with the background and would introduce regular errors in the spatial phase estimation. These ghost beams have been observed at the output of the AOM when an RF mixer was used to multiply the drive frequencies, as was the case for this measurement. Recent tests indicate that the AD835 active multiplier produces a much cleaner drive signal, and will likely replace the mixer in the next implementation of the acousto-optic projector.

Perhaps most striking, however, is the presence of "canyons" on the reconstructed surface. Unlike the noise present in the shadowed regions, these features are clearly not due to large random errors in phase measurement, but are due to errors in phase unwrapping. Examination of the unwrapped phase-maps reveals that while the 6MHz phase-map is unwrapped correctly resulting in a smooth phase variation, the 40MHz phase-map exhibits jumps in phase corresponding to the locations of the canyons. This leads one to conclude that the phase resolution in the suspect areas of the 6MHz phase-map is not good enough to disambiguate 360° jumps in the 40MHz phase-map. As explained in Chapter 2, it is this kind of behavior that ultimately determines how many sets of reference fringes are needed to unwrap a high-resolution phase-map, and what frequency ratios should be used. In this case, changing the difference frequency for the second reference phase-map from 6MHz to 8MHz, for example, may result in a better unwrapping. The signal-to-noise ratio, and hence phase resolution, can also be improved by increasing the contrast of the fringes by pulsing the laser with a shorter duty cycle

square wave and by increasing the available dynamic range in the manner described above.

It may not be even necessary, however, to unwrap the 40MHz phase-map. For many 3D applications resolving sub-millimeter indentations on an object is not required, but a representation of the overall shape of the object is desired instead. For such applications, imaging fringes produced with 1MHz and 6MHz difference frequencies, for example, would be sufficient to determine the overall shape of the golf ball, and would result in 33% increase in data acquisition rate. Figure 4.6 shows a 3D reconstruction of a LEGO™ knob made with 2MHz and 10MHz difference frequencies, and thus six frames in total. If one's goal is resolve the letters on the stud, clearly 10MHz fringes provide sufficient resolution.

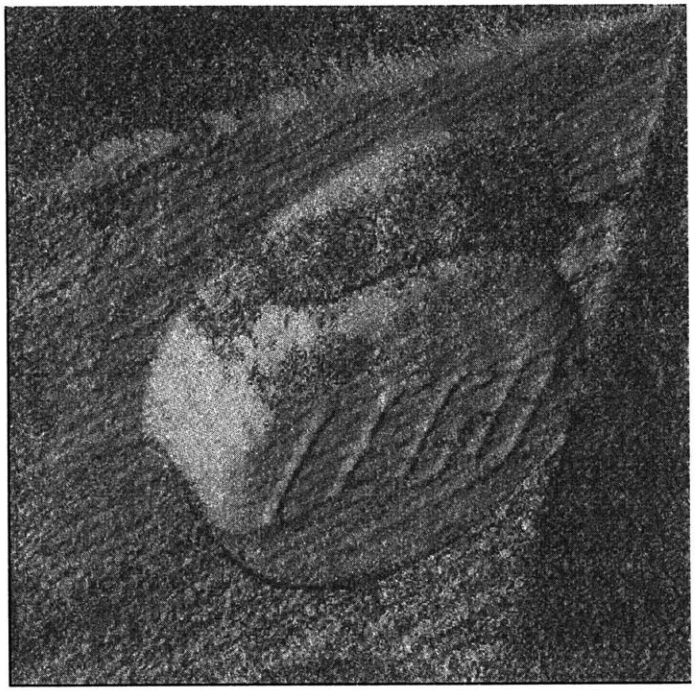

Figure 4.6 Reconstruction of a LEGO™ stub using only six CCD frames

Chapter 5

Conclusions

The previous chapters have discussed and demonstrated how acousto-optics can be used in an Accordion Fringe Interferometry system to acquire the data necessary to reconstruct the 3D surface of an object at video-rates and faster. Listed below are some ideas for future projects that can help transform acousto-optic AFI from a proof of concept into a useful and novel 3D imaging system.

Making acousto-optic AFI portable and inexpensive:

The optics of an acousto-optic AFI system consist of a diode laser, a crystal, a lens, and a CCD camera. It is easy to envision all of these solid-state components miniaturized and fitted into a pill box, or even printed onto a machine-vision circuit board.

Ironically, the largest and most expensive components of the *implemented* AFI system are the RF electronics. However, an expensive arbitrary waveform generator, which was used for maximum flexibility in the laboratory, is not necessary to control the phase and frequency of the fringe pattern for the purposes of AFI. In fact, it can be

replaced without sacrifice with a VLSI Direct Digital Synthesis integrated circuit, such as the Qualcomm Q2368 (which is currently priced at about $16). The Q2368 can synthesize a single sinusoid with a 130MHz sampling clock, or two independently-controlled sinusoids using a 65MHz sampling clock, and uses 32 bits to encode both frequency and phase of the synthesized waveform. A high-speed DAC is needed to convert its 12-bit output into an analog waveform. A design of AOM control electronics using the Q2368 chip is shown in Figure 5.1. Furthermore, a compact 1.5 Watt RF amplifier can be designed [18] to amplify the RF output of the DDS system to the levels necessary to drive the AOM.

Making a video-rate acousto-optic AFI system:

The speed of an acousto-optic AFI system is limited by the frame rate of the detector, since the projector can update the fringe pattern close to a million times per second. Although the implemented system is already capable of reconstructing nearly 100 surface maps per second by running a 256x256 CCD camera at almost 1000 fps, it is desirable to be able to achieve high 3D reconstruction rates with less exotic cameras. Two parallel roads can be pursued towards achieving this goal: minimizing the number of frames necessary to reconstruct the surface of an object to reduce the latency of the system, and studying the effects of pipelining CCD frames to increase the throughput. Statistical analysis [19], can be used to rigorously optimize the sampling of the fringe space.

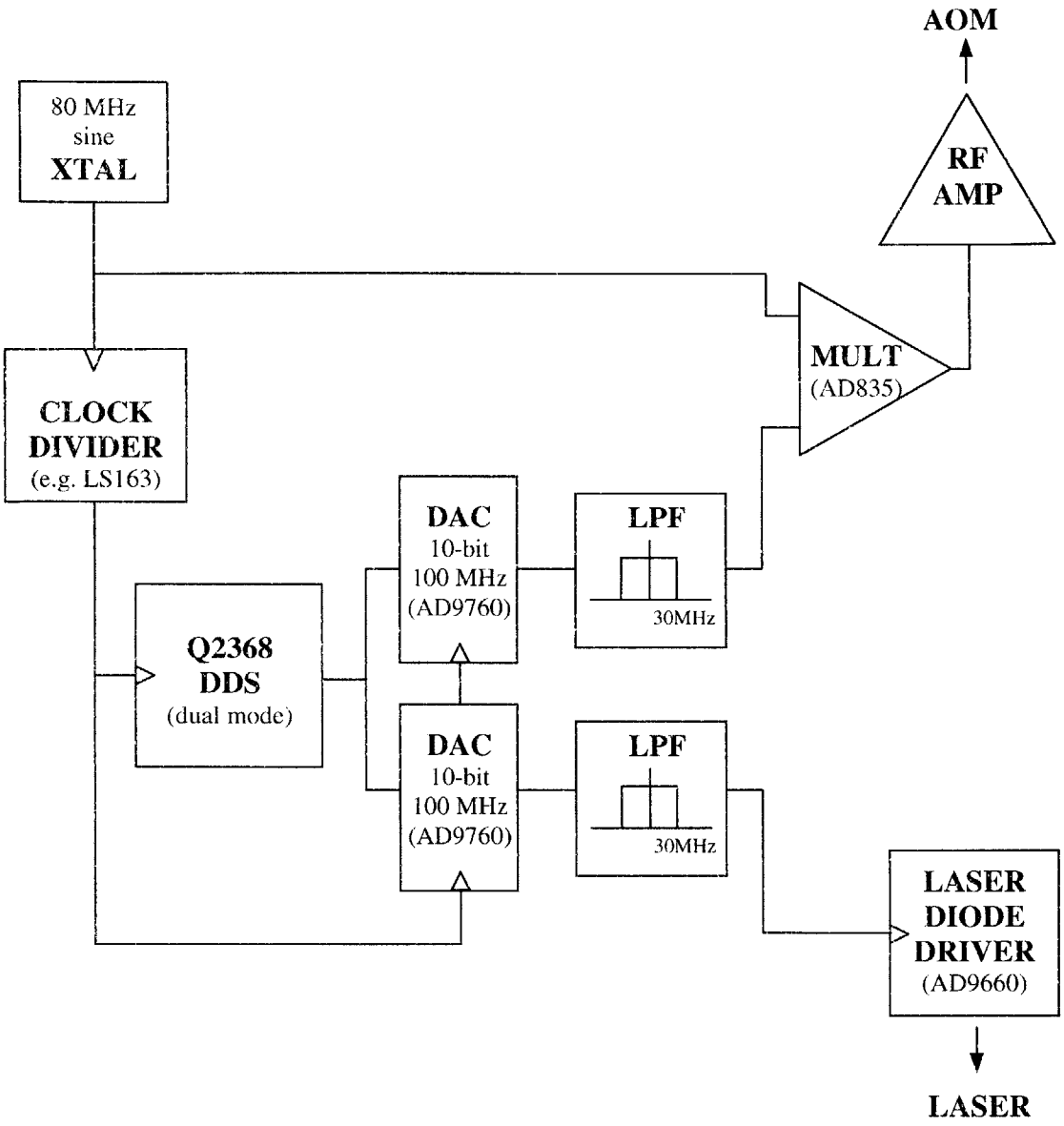

Figure 5.1 RF drive electronics using Qualcomm Q2368 DDS integrated circuit

Although fast 3D acquisition is clearly possible with a fast enough detector, applications such as machine vision, or quality control on a fast conveyor belt may require real-time processing of the data as well. While the ~4s processing time required to reconstruct a surface in Matlab on a 133MHz Pentium machine is very encouraging, the performance possible with dedicated DSP-based hardware[9] is not yet clear. Because of the pixel-independent nature of the AFI technique, parallel processing approaches may improve processing time tremendously.

Taking advantage of the AOM's modulation bandwidth:

While the image acquisition rate of the AFI system is limited by the frame rate of the detector, one can still take advantage of the high update speed of the acousto-optic projector. By interfacing the AOM with a variety of sensors via a high-speed feedback system, for example, it may be possible to actively compensate for the effects of vibration or high-frequency turbulence in the atmosphere, which are detrimental not just for high-speed AFI, but for a number of interferometry techniques that rely on projecting interference fringe patterns[10].

Designing a sensory aid for the blind:

A particularly inspiring and helpful application for a high speed 3D imaging system is a novel sensory aid for the blind. A portable device comprised of a video-rate AFI system interfaced with a high-bandwidth tactile display, may allow a blind person to navigate and recognize remote objects by feeling a rapidly-updated 3D model of the

[9] A programmable DSP board geared for video-rate processing for machine vision applications is available from Digital Designs of Cambridge, MA.

environment with his or her fingertips. Such an acousto-optic AFI system can illuminate and image the volume of a small room from several meters away using a 100mW IR laser, for example, offering a significant extension to the range and the bandwidth of a walking cane[11].

This thesis has demonstrated that a solid-state acousto-optic interference fringe projector is a practical device and can be interfaced with a high-speed imager in a 3D measurement system that is fast, robust, accurate, repeatable, portable, and economical. It is the author's hope that this work will help bring Accordion Fringe Interferometry into the world of entertainment, medicine, and research and help advance our ability to exchange 3D information in the course of our everyday lives.

[10] See for example proposal for active control of antenna surfaces [20]
[11] Professor Kenneth Salisbury of the Artificial Intelligence laboratory at MIT is currently conducting research in the field of tactile interfaces.

Appendix A: An Implementation of the AFI Algorithm

```
% this scripts places a surface in sumulated space using the peaks function,
% projects two sets of fringes onto it (large reference fringes, and fine fringes),
% reconstructs the surface using phase measurement and triangulation,
% and plots the surface
%
% the siumulated fringes are quantized using 256 levels
% no noise is added to the fringes in this case
% shadows are not simulated
%
% the geometric parameters are as follows:
%
% distance of object center from CCD:                50cm
% maximum range extent of object:                    5cm
%
% lambda=685 nm
% alpha=pi/4.2
% r=-476 mm
% b=370 mm
% delta=pi/104
%
% point source separations used:
%               reference:              a=0.0005 mm
%               fine:                   a=.178 mm

t0=clock;
hmap=peaks(256);
hmap=stretch(hmap,256);
hmap=putheader(hmap,'lambda',0.000685,'a',.178,'alpha',pi/4.2,'r',-
426,'b',370,'delta',pi/104);
fr1=fringepaint(hmap,-pi/4,0.195,792,256,0,0);
fr2=fringepaint(hmap,0,0.195,792,256,0,0);
fr3=fringepaint(hmap,pi/4,0.195,792,256,0,0);
pmap=phasemap(fr1,fr2,fr3);
hmap=(putheader(hmap,'a',0.0005));
fr1ref=fringepaint(hmap,-pi/4,0.195,792,256,0,0);
fr2ref=fringepaint(hmap,0,0.195,792,256,0,0);
fr3ref=fringepaint(hmap,pi/4,0.195,792,256,0,0);
pmapref=phasemap(fr1ref,fr2ref,fr3ref);
n=p2n(pmap,pmapref,copyheader(zeros(256),pmapref));
z=p2z(pmap,n);
surfl(stretch(z(2:end,:),256));shading interp; colormap gray
etime(clock,t0)
```

```
function fringes=fringepaint(hmap,phase,zscale,zdist,signal,bkg,noise);
% fringepaint(hmap,zscale,zdist,signal,bkg,noise);
% maps a 2-d image, hmap, into xyz-space based on the level (hmap must have a header)
% paints the xyz-space with fringes to simulate data
%
% - phase of the cos^2 fringe function (note, 90° shift in cos = 45° shift in cos^2)
% - zscale is in mm/(hmap unit)
%    the higher the hmap, the closer to camera
% - zdist is the distance from the CCD to the surface at center of f.o.v. (mm)
% - signal is the number of levels of the projected fringe pattern
% - bkg is the number of levels of the noise floor
% - noise is the MAGNITUDE of the maximum random noise level
%
%
% to see header variables, type "help headertable"

lambda=getheader(hmap,'lambda');
a=getheader(hmap,'a');
alpha=getheader(hmap,'alpha');
r=getheader(hmap,'r');
b=getheader(hmap,'b');
delta=getheader(hmap,'delta');
```

```
fringes=hmap;
% remove header
hmap=hmap(2:end,:);

len=size(hmap,2);
height=size(hmap,1);
midpointx=round(len/2);
midpointy=round(height/2);
z=zdist+zscale.*(hmap(midpointy,midpointx)-hmap);
indexesx=[1:len];
indexesy=[1:height];
[x dummy]=meshgrid(indexesx,indexesy);
clear dummy;

% do reverse-triangulation
tanbeta=tan((x-midpointx)/midpointx*delta);
x=z.*tanbeta;
y=(z+r-(b-x)*tan(alpha))*cos(alpha);
s=(z+r-y*cos(alpha))/sin(alpha);

% generate additive phase noise
nz=0;
if (noise ~= 0)
   nz=floor((0.5-rand(height,len))*2*noise);
end;

% implement I=I0*cos^2(y*a*pi/(s*lambda))
fringes(2:end,:)=floor((signal-1)*(cos(a*pi/lambda*y./s+phase)).^2)+nz+floor(bkg);
```

```
function p=phasemap(I1,I2,I3);
% phasemap(I1,I2,I3);
% calculates phase based on three measurements of the fringe sinusiod 90° apart
% note: order of phasemaps is important: I1=-90°, I2=0°, I3=90°
%
% to see header variables, type "help headertable"

% copy header
p=I1;

%strip headers
I1=I1(2:end,:);
I2=I2(2:end,:);
I3=I3(2:end,:);

p(2:end,:)=atan2((I1-I3),(2*I2-I1-I3))./2;
```

```
function n=p2n(p,pref,nref);
% p2n(p,pref,nref);
% calculates a fringe-number n for each pixel based on reference phase-map
% fringe numbers are used to unwrap the phasemap later
%
% to see header variables, type "help headertable"

%copy header
n=p;

a=getheader(p,'a');

if (getheader(pref,'id') ~= getheader(nref,'id'))
   warning('Pref and Nref have different session IDs')
end
if (getheader(pref,'a') ~= getheader(nref,'a'))
   warning('Pref and Nref have different source separations')
end

aref=getheader(pref,'a');

%strip headers
p=p(2:end,:);
pref=pref(2:end,:);
nref=nref(2:end,:);

n(2:end,:)=round((a/aref*(pref+nref*pi)-p)./pi);
```

```
function z=p2z(p,n);
% p2z(p,n);
% calculates depth map from the wrapped phasemap and fringe numbers
% (see Figure 4.1 in text for derivation of triangulatin formulas)
%
% to see header variables, type "help headertable"

lambda=getheader(p,'lambda');
a=getheader(p,'a');
alpha=getheader(p,'alpha');
r=getheader(p,'r');
b=getheader(p,'b');
delta=getheader(p,'delta');

if (getheader(p,'id') ~= getheader(n,'id'))
   warning('P and N have different session IDs');
end

if (getheader(p,'a') ~= getheader(n,'a'))
   warning('P and N have different source separations');
end


sina=sin(alpha);
cosa=cos(alpha);

z=p;

%strip headers
p=p(2:end,:);
n=n(2:end,:);

tantheta=(p+n*pi)*lambda/(a*pi);
len=size(p,2);
midpointx=round(len/2);

xpix=p;
for i=1:len
   xpix(:,i)=i-midpointx;
end;

tanbeta=tan(xpix/(midpointx/delta));

z(2:end,:)=(r.*tantheta+(b*sina-
r*cosa).*(tantheta.*cosa+sina))./((tanbeta.*sina+cosa).*(tantheta.*cosa+sina)-tantheta);
```

```
function names=headertable();
% headertable();
% returns a cell array of variable names, in the order as they appear in header
%
% THE HEADER FOLLOWS THE FOLLOWING FORMAT:
% header is the first row of matrix, and is as follows:
% columns in increasing order:
% 1-6: tag     ='header' (used to distinguish matrixes with headers from raw matrixes)
% 7: ID        =this is the non-zero ID of the session
% 8: lambda    =laser wavelength (mm)
% 9: a         =source separation (mm)
% 10: alpha    =angle between source and detector normals (rad)
% 11: r        =distance from CCD plane to source midpoint (away from object) (mm)
% 12: b        =baseline between the ccd center and the source midpoint projection onto
ccd plane (mm)
% 13: delta    =halfangle f.o.v. of lens (rad)


names={'id' 'lambda' 'a' 'alpha' 'r' 'b' 'delta'};
```

```
f unction value=getheader(mat,name)
% getheader(mat,name)
% returns the value of the desired header variable
%
% to see header variables, type "help headertable"

names=headertable;
tag=double('header');

if (mat(1,1:6) ~= tag)
   error('This matrix does not have a header.  Aborting.')
```

```
end;

found=0;

for j=1:length(names)
   if (strcmp(name,names(j)))
      value=mat(1,(length(tag)+j));
      found=1;
   end;
end;
if (found == 0)
   sprintf('!!!Warning!!! variable "%s" not found in header',name)
end;
```

```
function mat=putheader(mat,varargin);
% putheader(mat,varargin);
% assigns a value to the desired header variable(s)
% varargin format: 'name',value,'name',value, etc...
%
% to see header variables, type "help headertable"

if (mod(length(varargin),2) ~= 0)
   error('Incorrect number of arguments.  Aborting.')
end;

names=headertable;
tag=double('header');

% if mat has no header, create one
if (mat(1,1:6) ~= tag)
   tempmat=mat;
   mat=zeros(size(mat,1)+1,size(mat,2));
   mat(1,1:6)=tag;
   mat(2:end,:)=tempmat;
   clear tempmat;
end;

found=0;

for i=1:2:length(varargin)
   for j=1:length(names)
      if (strcmp(varargin{i},names(j)))
         mat(1,(length(tag)+j))=varargin{i+1};
         found=1;
      end;
   end;
   if (found == 0)
      sprintf('!!!Warning!!! variable "%s" not found in header',varargin{i})
   end;
end;
```

```
function host=copyheader(host,donor)
% hosth=copyheader(host,donor);
% copies the header from the donor to the host
% host does not have to have a header
%
% to see header variables, type "help headertable"

tag=double('header');

if (donor(1,1:6) ~= tag)
   error('Donor does not have a header.  Aborting.')
end;


% if host has no header, create one
if (host(1,1:6) ~= tag)
   temphost=host;
   host=zeros(size(host,1)+1,size(host,2));
   host(1,:)=donor(1,:);
   host(2:end,:)=temphost;
   clear temphost;

% otherwise, just copy header
else
   host(1,:)=donor(1,:);
end;
```

Bibliography

[1] L.G. Shirley, "Three-Dimensional Imaging using Accordion Fringe Interferometry", to be published, Applied Optics

[2] L.G.Shirley, "Accordion Fringe Interferometry: A Novel 3D Imaging Technique", *MIT Lincoln Laboratory Staff Seminar*, 31 January 1997.

[3] Sumit Basu, "A Three-Dimensional Model of Human Lip Motion", Master's Thesis, Massachussets Institute Of Technology, Department of Electrical Engineering and Computer Science, 1997.

[4] Joseph Karlin, "3D Imaiging methods for manufacturing, with Emphasis on the Laser Speckle Technique", Master's Thesis, Massachussets Institute Of Technology, Department of Mechanical Engineering, 1995.

[5] D. Nitzan, "Three-Dimensional vision structure for robot applications", *IEEE Transactions on Pattern Analysis and Machine Intelligence*, Vol. 10, No.3, May 1988.

[6] D. Svetkoff, "Towards a High Resolution, Video Rate, 3D Sensor for Machine Vision", *SPIE*, vol 728, 1986.

[7] Paul J. Besl, "Active, Optical Range Imaging Sensors", in Saanz, Jorge L.C., ed., *Advances in Machine Vision*, Springer-Verlag, New York, Chapter 1, 1989, pp1-63.

[8] Lyle G. Shirley, Emory D. Ariel, Gregory R.Hallerman, Harold C. Payson, and John R. Vivilecchia, "Advanced techniques for target Discrimination Using Laser Speckle", *MIT Lincoln Laboratory Journal,* Vol. 5, No. 3, Fall 1992.

[9] Lyle G. Shirley, Gregory R.Hallerman "Applications of tunable Lasers to Laser Radar and 3D Imaging", *MIT Lincoln Laboratory Technical Report No. 1025*, 26 february 1996

[10] John M. Fini, "Three Dimensional Image Reconstruction from Fourier Magnitude Measurements", Master's Thesis, Massachussets Institute Of Technology, Department of Electrical Engineering and Computer Science, 1997.

[11] Michael S. Mermelstein, "A Large-Scale Three-Dimensional Imaging System Based On Laser Speckle", Master's Thesis, Massachussets Institute Of Technology, Department of Electrical Engineering and Computer Science, 1995.

[12] Eugene Hecht, *Optics* , 2nd Edition, Addison-Welseley Publishing Co., ©1987

[13] Brillouin, L., "Diffusion de la Lumière et des Rayons X par un Corps Transparent Homogène," Ann. Physique, 1922, pp17-88

[14] Amnon Yariv, *Optical Electronics in Modern Communications*, 5th Edition, Oxford University Press, 198 Madison Avenue, New York, ©1997, pp 474-489, pp 50-56

[15] C.V Raman, N.S.N. Nath, "The Diffraction of Light by High Frequency Sound Waves: part II," *Proc. Indian. Sci.*, Vol. 2, 1935, pp 413-420

[16] W.R. Klein, W. D. Cook, "Unified Approach to Ultrasonic Light Diffraction", *IEEE Transactions on Sonics and Ultrasonics*, Vol. SU-14, No. 3, July 1967, pp 123-134.

[17] *Isomet* technical documentation on acousto-optic devices, 1998

[18] Paul Horowitz, Winfield Hill, *The Art of Electronics*, 2nd Ed., Cambridge University Press, ©1989, pp 863-888.

[19] Philip R. Bevington, D.Keith Robinson, *Data Reduction and Error Analysis for the Physical Sciences*, McGraw-Hill, Inc., ©1992

[20] LyleG. Shirley, "Optical Sensor for Active Control of Antenna Surfaces"